

An efficient asymptotic preserving Monte Carlo method for frequency-dependent radiative transfer equations

Yiyang Hong^a, Yi Shi^b, Yi Cai^a, Tao Xiong^{c,*}

^a*School of Mathematical Sciences, Xiamen University, Xiamen, Fujian 361005, PR China*

^b*School of Mathematics, Shandong University, Jinan, Shandong 250100, PR China*

^c*School of Mathematical Sciences, University of Science and Technology of China, Hefei, Anhui 230026, PR China*

Abstract

In this paper, we develop an efficient asymptotic-preserving (AP) Monte Carlo (MC) method for frequency-dependent radiative transfer equations (RTEs), which is based on the AP-MC method proposed for the gray RTEs in [1]. We follow the characteristics-based approach by Zhang et al. [2] to get a reformulated model, which couples a low dimension convection-diffusion-type equation for macroscopic quantities with a high dimension transport equation for the radiative intensity. To recover the correct free streaming limit due to frequency-dependency, we propose a correction to the reformulated macroscopic equation. The macroscopic system is solved using a hybrid method: convective fluxes are handled by a particle-based MC method, while diffusive fluxes are treated implicitly with central difference. To address the nonlinear coupling between radiative intensity and the Planck function across multiple frequency groups, we adopt a Picard iteration with a predictor-corrector procedure, which decouples a global nonlinear system into a linear system restricted to spatial dimension (independent of frequency) with scalar algebraic nonlinear equations. Once the macroscopic update is done, the transport equation—with a known emission source provided by the macroscopic variables—is efficiently solved using an implicit MC method. This approach enables larger time steps independent of the speed of light and also the frequency across a wide range, significantly enhancing computational efficiency, especially for frequency-dependent RTEs. Formal AP analysis in the diffusive scaling is established. Numerical experiments are performed to demonstrate the high efficiency and AP property of the proposed method.

Keywords: Frequency-dependent; Radiative transfer equations; Monte Carlo; Asymptotic preserving.

1. Introduction

The radiative transfer equations (RTEs) are fundamental in modeling photon transport and interactions with matter in high-energy-density systems, such as astrophysics, inertial confinement fusion (ICF) and high-temperature flows. Their solution is challenging due to the high dimensionality, strong nonlinear coupling, and multiscale behavior in both space and

*Corresponding author.

Email addresses: hongyy23@stu.xmu.edu.cn (Yiyang Hong), shiyi@sdu.edu.cn (Yi Shi), yicaim@stu.xmu.edu.cn (Yi Cai), taoxiong@ustc.edu.cn (Tao Xiong)

time. It has attracted a lot of attention for numerical studies because of its importance but high complexity.

A popular strategy for simulating the RTEs is the deterministic method, which includes the spherical harmonic (also known as the P_N) and the discrete ordinate (also known as the S_N) methods. In the P_N approximation [3, 4, 5, 6], the radiation intensity is decomposed into a series of angular moments to arrive at a finite hyperbolic system. In the S_N approximation [3, 4, 7, 8, 9], the intensity is divided into certain selected directions, and a system of coupled discrete equations should be solved. However, each method has its limitations [10]: the S_N method suffers from *ray effects*, while the P_N method is prone to *wave effects* in time-dependent problems.

An alternative approach is the stochastic method, such as the Monte Carlo (MC) method. MC methods allow for continuous treatment of phase-space variables during particle tracking. Despite inherent statistical fluctuations, they are highly flexible, especially for complex geometries, and are free from ray effects or wave effects. The implicit Monte Carlo (IMC) method [11] is an important stochastic approach for solving RTEs. It treats absorption and emission semi-implicitly via effective scattering, improving stability, and allowing for larger time steps compared to fully explicit MC methods. However, in optically thick regime with short photon mean free paths, particles undergo many collisions due to effective scattering, resulting in high computational cost and reduced efficiency. Efforts have been made to improve the efficiency of the IMC method in optically thick regions, such as the random walk approach [12, 13, 14], discrete diffusion Monte Carlo (DDMC) methods [15, 16], and implicit Monte Carlo diffusion (IMD) methods [17, 18, 19]. The DDMC methods and IMD methods are transport-diffusion hybrid methods which simulate the RTEs with a diffusion approximation in optically thick regions and the standard IMC method in other regions. Special efforts need to be made for domain decomposition and information exchange at transport-diffusion interfaces [20].

Gray radiative transfer equations (GRTEs) are a type of simplified RTEs, where the opacity depends solely on the material type or material temperature. This enables spatial partitioning into optically thick and thin regions, allowing for the use of different numerical methods in each. In frequency-dependent radiative transfer equations (FRTEs), opacity typically decreases with frequency, making a region optically thick at low frequencies but thin at high ones. This frequency dependence presents significant mathematical and numerical challenges, particularly in consistently coupling diffusion-like and free-streaming behaviors across the entire computational domain. One effective approach to address these challenges is the moment-based acceleration scheme known as the High-Order/Low-Order (HOLO) algorithm [21, 22, 23, 24]. In the HOLO algorithm, a low-order system — comprising the first two moments of the RTEs coupled with the material temperature equation is solved first. The solution from this low-order system is then used to determine the Planckian emission source term, which is subsequently employed to solve the RTEs. The benefit of HOLO algorithms lies in their ability to eliminate nonlinearity, however, ensuring long-term accuracy and nonlinear stability requires maintaining discrete consistency between the HO and LO formulations [21]. Another efficient approach to deal with these difficulties is the asymptotic preserving (AP) scheme. This approach has its origin in capturing steady-state solution for neutron transport in the diffusive regime [25, 26], and later applied to non-stationary transport problems [27]. The basic idea behind AP schemes is to ensure that the numerical method accurately captures the asymptotic limit of the mathematical model at the discrete level [28], avoiding dealing with the transport-diffusion interfaces in the domain decomposition method. There are various ways to construct an AP scheme for RTEs, including micro-macro decomposition [1, 2, 9], unified gas kinetic

(UGK) method [8, 29, 30, 31, 32, 33, 34, 35], three-state update method [36], AP-HOLO [37], linear-discontinuous spatial differencing scheme [38], etc and some of them have been extended to FRTEs.

In this work, we aim to develop an efficient AP MC method for FRTEs. For the frequency variable, we employ the classical multi-group approach [3]. In this approach, the frequency variable is discretized into a finite number of groups and the frequency integration is only performed over the groups. Building on the idea originally proposed in the UGK scheme [39, 40], we substitute, for each group, an integral solution that traces the characteristics of the microscopic transport equation to construct the flux for the corresponding macroscopic radiation energy equation. Unlike UGK-type methods, which numerically approximate the macroscopic radiative flux based on information from neighboring cells, we adopt a characteristics-based approach [2], wherein we further perform integration by parts and suitably approximate the resulting integrals along the characteristic lines to close the macroscopic flux. This approximation can be formally shown to be of order $O(\Delta t^2)$ for linear kinetic model [2, 41]. The resulting macroscopic equation incorporates long-range characteristic tracing, which enables the use of larger time steps independent of the speed of light. To address model approximation errors in the free-streaming regime, we introduce a correction to the original model. We then adopt a hybrid finite volume method for solving the macroscopic system: the convective flux is computed using the particle-based MC method, while the diffusive flux is handled implicitly with central difference. The new challenge for FRTEs is the nonlinear coupling between the group-wise radiative intensity and the group-wise Planck function, which results in a high-dimensional implicit system that involves not only spatial variables but also the frequency (group) dimension. Instead of employing the linearized iterative solver from [30, 8], as used in our previous work [1], we adopt a Picard iteration with the predictor-corrector procedure proposed in [36] to efficiently manage this group-wise nonlinearity. The solution of the global nonlinear system is divided into two stages: a predictor step that solves a linear system and decouples the frequency dimension, followed by a corrector step that solves nonlinear scalar equations locally within each spatial cell. This predictor-corrector process is iterated until convergence within each Picard iteration. Notably, in our scheme, the linear system involves a matrix whose size depends only on the number of spatial cells, allowing for efficient computation. Once the macroscopic equation is solved, the updated material temperature provides an *a priori* estimate for the Planckian emission source. This reduces the transport equation to a purely absorbing problem with a known source, which can be directly solved using MC method. To mitigate the so-called *teleportation error* [12], we extend the continuous source tilting technique from [42] to FRTEs, preserving the correct equilibrium diffusion limit. Formal AP analysis in the diffusive scaling is established. Numerical experiments demonstrate that the proposed method is significantly more efficient than the IMC method [11], particularly in optically thick regime.

The rest of the paper is organized as follows. In Section 2, we revisit the model equations and derive the approximation model in the general multi-dimensional case. The numerical methods for the approximation model are described in Section 3. Formal asymptotic analysis are given in Section 4. We provide some numerical tests in Section 5, followed by a conclusion remark in Section 6.

2. Model approximation and reformulation

The frequency-dependent radiative transfer equations in the absence of material motion, scattering, heat conduction, and internal sources can be written as [43]

$$\frac{1}{c} \frac{\partial I}{\partial t} + \boldsymbol{\Omega} \cdot \nabla I = \sigma(B - I), \quad (2.1a)$$

$$\frac{\partial u_m}{\partial t} = \int_0^\infty \int_{4\pi} \sigma(I - B) d\boldsymbol{\Omega} d\nu, \quad (2.1b)$$

with the prescribed initial conditions

$$I(\mathbf{x}, \boldsymbol{\Omega}, \nu, 0) = I^i(\mathbf{x}, \boldsymbol{\Omega}, \nu), \quad (2.2a)$$

$$T(\mathbf{x}, 0) = T^i(\mathbf{x}), \quad (2.2b)$$

and the prescribed inflow boundary conditions

$$I(\mathbf{x}, \boldsymbol{\Omega}, \nu, t) \Big|_{\mathbf{x} \in \partial V} = I_{bc}(\mathbf{x}, \boldsymbol{\Omega}, \nu, t), \quad \boldsymbol{\Omega} \cdot \mathbf{n} < 0. \quad (2.3)$$

This system describes the radiative transfer and energy exchange between the radiation and the material. Here, $\mathbf{x} \in V \subset \mathbb{R}^3$ is the spatial variable on a specified physical domain V , $\boldsymbol{\Omega} \in \mathbb{S}^2$ is the angular variable on the unit sphere \mathbb{S}^2 , $\nu \in \mathbb{R}^+$ is the frequency variable, $t \in \mathbb{R}^+$ is the temporal variable, \mathbf{n} is the unit outward normal vector on ∂V , $u_m(T)$ is the material energy density, $\sigma(\mathbf{x}, \nu, T)$ is the opacity of the material, and c is the speed of light. The two main unknowns are:

$I(\mathbf{x}, \boldsymbol{\Omega}, \nu, t)$ = the radiation intensity,

$T(\mathbf{x}, t)$ = the material temperature.

The Planck function $B(\nu, T)$ is defined as

$$B(\nu, T) = \frac{2h\nu^3}{c^2} \frac{1}{e^{h\nu/kT} - 1}, \quad (2.4)$$

with the Boltzmann's constant k and the Planck's constant h . The function $B(\nu, T)$ satisfies

$$\int_0^\infty B(\nu, T) d\nu = \frac{1}{4\pi} acT^4, \quad (2.5)$$

where $a = \frac{8\pi^5 k^4}{15h^3 c^3}$ is the radiation constant. The normalized Planck function $b(\nu, T)$ is defined by

$$b(\nu, T) = \frac{B(\nu, T)}{\int_0^\infty B(\nu, T) d\nu} = \frac{4\pi}{acT^4} B(\nu, T), \quad (2.6)$$

thus we have $\int_0^\infty b(\nu, T) d\nu = 1$. The material energy density u_m is related to the material temperature T through the following equation of state

$$\frac{\partial u_m}{\partial T} = C_v(\mathbf{x}, T), \quad (2.7)$$

where C_v is the heat capacity of material. For simplicity, in this work, it is assumed that C_v is independent of the material temperature T , and we use the relation

$$\frac{\partial u_m}{\partial t} = C_v \frac{\partial T}{\partial t}, \quad (2.8)$$

in our subsequent discussion.

The spatial variable \mathbf{x} is usually presented by the Cartesian coordinate with $\mathbf{x} = (x, y, z)$, while the angular variable $\boldsymbol{\Omega}$ is given by the spherical coordinates (θ, φ) with polar angle $\theta \in [0, \pi]$ and azimuthal angle $\varphi \in [0, 2\pi]$, then

$$\boldsymbol{\Omega} = (\xi, \eta, \mu), \quad \mu = -\cos \theta, \quad \xi = \sin \theta \cos \varphi, \quad \eta = \sin \theta \sin \varphi,$$

and

$$d\mathbf{x} = dx dy dz, \quad d\boldsymbol{\Omega} = \sin \theta d\theta d\varphi = d\mu d\varphi.$$

In the one-dimensional (1D) case, (2.1) reduces to

$$\begin{aligned} \frac{1}{c} \frac{\partial I}{\partial t} + \mu \frac{\partial I}{\partial x} &= \sigma(B - I), \\ C_v \frac{\partial T}{\partial t} &= 2\pi \int_0^\infty \int_{-1}^1 \sigma(I - B) d\mu d\nu, \end{aligned} \quad (2.9)$$

with $\mu \in [-1, 1]$, note that here we use x to replace z for convenience. While in the two-dimensional (2D) case, it becomes

$$\begin{aligned} \frac{1}{c} \frac{\partial I}{\partial t} + \xi \frac{\partial I}{\partial x} + \eta \frac{\partial I}{\partial y} &= \sigma(B - I), \\ C_v \frac{\partial T}{\partial t} &= \int_0^\infty \int_0^{2\pi} \int_{-1}^1 \sigma(I - B) d\mu d\varphi d\nu, \end{aligned} \quad (2.10)$$

with

$$\xi = \sqrt{1 - \mu^2} \cos \varphi \in [-1, 1], \quad \eta = \sqrt{1 - \mu^2} \sin \varphi \in [-1, 1], \quad \mu \in [-1, 1], \quad \varphi \in [0, 2\pi].$$

2.1. The Multi-group method

Using the multi-group method, the continuous frequency space $(0, \infty)$ is divided into G groups, where all photons within a given group are treated with a single representative frequency, assigning an averaged opacity. The frequency interval is denoted by $(\nu_{g-\frac{1}{2}}, \nu_{g+\frac{1}{2}})$ for $g = 1, \dots, G$, with $\nu_{\frac{1}{2}} = 0$ and $\nu_{G+\frac{1}{2}} = \infty$. In practice, a cutoff frequency of $\nu_{\frac{1}{2}}$ and $\nu_{G+\frac{1}{2}}$ is usually taken, which will be specified in the numerical tests. For each $g = 1, \dots, G$, we define the group-wise radiation intensity I_g and Planck function B_g as the integral over the frequency interval $(\nu_{g-\frac{1}{2}}, \nu_{g+\frac{1}{2}})$:

$$I_g(\mathbf{x}, \boldsymbol{\Omega}, t) := \int_{\nu_{g-\frac{1}{2}}}^{\nu_{g+\frac{1}{2}}} I(\mathbf{x}, \boldsymbol{\Omega}, \nu, t) d\nu, \quad (2.11a)$$

$$B_g(T) := \int_{\nu_{g-\frac{1}{2}}}^{\nu_{g+\frac{1}{2}}} B(\nu, T) d\nu. \quad (2.11b)$$

With this definition, we can rewrite (2.1) as,

$$\frac{1}{c} \frac{\partial I_g}{\partial t} + \boldsymbol{\Omega} \cdot \nabla I_g = \sigma_g (B_g - I_g), \quad g = 1, \dots, G, \quad (2.12a)$$

$$C_v \frac{\partial T}{\partial t} = \sum_{g=1}^G \int_{4\pi} \sigma_g (I_g - B_g) d\boldsymbol{\Omega}, \quad (2.12b)$$

where a piecewise constant approximation is adopted for the group-wise opacity σ_g :

$$\sigma_g(\mathbf{x}, T) := \frac{\int_{\nu_{g-\frac{1}{2}}}^{\nu_{g+\frac{1}{2}}} \sigma(\mathbf{x}, \nu, T)(B - I) d\nu}{\int_{\nu_{g-\frac{1}{2}}}^{\nu_{g+\frac{1}{2}}} (B - I) d\nu} \approx \frac{\int_{\nu_{g-\frac{1}{2}}}^{\nu_{g+\frac{1}{2}}} \sigma(\mathbf{x}, \nu, T) d\nu}{\nu_{g+\frac{1}{2}} - \nu_{g-\frac{1}{2}}}. \quad (2.13)$$

For a detailed discussion on the approximation for σ_g , we refer readers to [3, 44]. The corresponding group-wise initial and boundary condition are given by:

$$\begin{aligned} I_g(\mathbf{x}, \Omega, 0) &= I_g^i(\mathbf{x}, \Omega) := \int_{\nu_{g-\frac{1}{2}}}^{\nu_{g+\frac{1}{2}}} I^i(\mathbf{x}, \Omega, \nu) d\nu, \\ I_g(\mathbf{x}, \Omega, t) \big|_{\mathbf{x} \in \partial V} &= I_{bc,g}(\mathbf{x}, \Omega, t) := \int_{\nu_{g-\frac{1}{2}}}^{\nu_{g+\frac{1}{2}}} I_{bc}(\mathbf{x}, \Omega, \nu, t) d\nu, \quad \Omega \cdot \mathbf{n} < 0. \end{aligned} \quad (2.14)$$

2.2. A semi-Lagrangian approximation

Now, we operate on (2.12a) with $\int_{4\pi}(\cdot) d\Omega$, the system for macroscopic variables can be expressed as:

$$\frac{1}{c} \frac{\partial \rho_g}{\partial t} + \nabla \cdot \int_{4\pi} \Omega I_g d\Omega = \sigma_g (4\pi B_g - \rho_g), \quad g = 1, \dots, G, \quad (2.15a)$$

$$C_v \frac{\partial T}{\partial t} = \sum_{g=1}^G \sigma_g (\rho_g - 4\pi B_g), \quad (2.15b)$$

where $\rho_g := \int_{4\pi} I_g d\Omega$.

The primary objective of this subsection is to utilize the integral form of the microscopic equation (2.12a) with suitable approximation to close the flux $\int_{4\pi} \Omega I_g d\Omega$ in the macroscopic equation (2.15a). This idea originally comes from the UGK scheme [39, 40]. Whereas UGK scheme reconstructs the emission source term using a local linear polynomial derived from neighboring cells, our approach directly obtains the macroscopic flux through integration by parts of the time integral, combined with a semi-Lagrangian approximation [1, 2, 41]. This approach enables the use of a larger time step, which can be independent of the speed of light.

For each $g = 1, \dots, G$, we rewrite the microscopic equation (2.12a) into the following characteristic form

$$\frac{dI_g}{dt} = c\sigma_g(B_g - I_g), \quad (2.16a)$$

$$\frac{d\mathbf{x}}{dt} = c\Omega, \quad (2.16b)$$

with d/dt being a material derivative. Without loss of generality, we formally impose a time interval $[t^n, t^{n+1}]$. Starting from (\mathbf{x}, t) with $t \in [t^n, t^{n+1}]$, a backward tracing of the characteristic line is given by:

$$\mathbf{X}(s, \Omega; \mathbf{x}, t) = \mathbf{x} - c\Omega(t - s), \quad \forall s \in [t^n, t]. \quad (2.17)$$

For simplicity, we denote $\mathbf{X}(s)$ as shorthand for $\mathbf{X}(s, \Omega; \mathbf{x}, t)$. By multiplying (2.16a) with an exponential factor $e^{c\sigma_g s}$ and integrating over $s \in [t^n, t]$, we obtain:

$$\begin{aligned} I_g(\mathbf{x}, \Omega, t) &= e^{-c\sigma_g(t-t^n)} I_g(\mathbf{X}(t^n), \Omega, t^n) \\ &\quad + \int_{t^n}^t e^{-c\sigma_g(t-s)} c\sigma_g B_g(\mathbf{X}(s), s) ds. \end{aligned} \quad (2.18)$$

Integrating by parts for the second term in (2.18), we get

$$\begin{aligned} \int_{t^n}^t e^{-c\sigma_g(t-s)} c\sigma_g B_g(\mathbf{X}(s), s) ds &= \left(B_g(\mathbf{x}, t) - e^{-c\sigma_g(t-t^n)} B_g(\mathbf{X}(t^n), t^n) \right. \\ &\quad \left. - \int_{t^n}^t e^{-c\sigma_g(t-s)} \frac{dB_g}{ds}(\mathbf{X}(s), s) ds \right), \end{aligned} \quad (2.19)$$

where the material derivative is given by

$$\frac{dB_g}{ds}(\mathbf{X}(s), s) = \frac{\partial B_g}{\partial s}(\mathbf{X}(s), s) + c\boldsymbol{\Omega} \cdot \nabla B_g(\mathbf{X}(s), s).$$

For the time integral in (2.19), we follow the idea in [1, 2, 41] to give the following approximation,

$$\begin{aligned} \int_{t^n}^t e^{-c\sigma_g(t-s)} \frac{dB_g}{ds}(\mathbf{X}(s), s) ds &\approx \int_{t^n}^t e^{-c\sigma_g(t-s)} ds \left(\frac{dB_g}{ds}(\mathbf{X}(s), s) \Big|_{s=t} \right) \\ &= \frac{1}{c\sigma_g} (1 - e^{-c\sigma_g(t-t^n)}) \left(\frac{\partial B_g}{\partial s}(\mathbf{x}, t) + c\boldsymbol{\Omega} \cdot \nabla B_g(\mathbf{x}, t) \right). \end{aligned} \quad (2.20)$$

Together, we deduce

$$\begin{aligned} I_g(\mathbf{x}, \boldsymbol{\Omega}, t) &\approx e^{-c\sigma_g(t-t^n)} I_g(\mathbf{X}(t^n), \boldsymbol{\Omega}, t^n) \\ &\quad + \left(B_g(\mathbf{x}, t) - e^{-c\sigma_g(t-t^n)} B_g(\mathbf{X}(t^n), t^n) \right. \\ &\quad \left. - \frac{1}{c\sigma_g} (1 - e^{-c\sigma_g(t-t^n)}) \left(\frac{\partial B_g}{\partial s}(\mathbf{x}, t) + c\boldsymbol{\Omega} \cdot \nabla B_g(\mathbf{x}, t) \right) \right). \end{aligned} \quad (2.21)$$

By substituting (2.21) into the macroscopic equation (2.15a) to close the flux $\int_{4\pi} \boldsymbol{\Omega} I_g d\boldsymbol{\Omega}$, and using the definition of the characteristic line (2.17) (which indicates $\mathbf{X}(t^n)$ is angular-dependent), as well as the integrals $\int_{4\pi} \boldsymbol{\Omega} \cdot \mathbf{v} d\boldsymbol{\Omega} = 0$ and $\int_{4\pi} \boldsymbol{\Omega}(\boldsymbol{\Omega} \cdot \mathbf{v}) d\boldsymbol{\Omega} = \frac{4\pi}{3} \mathbf{v}$ for any variable \mathbf{v} that is angular-independent, we obtain

$$\begin{aligned} \frac{1}{c} \frac{\partial \rho_g}{\partial t} + \nabla \cdot \int_{4\pi} e^{-c\sigma_g(t-t^n)} \boldsymbol{\Omega} (I_g - B_g) (\mathbf{X}(t^n), \boldsymbol{\Omega}, t^n) d\boldsymbol{\Omega} \\ - \nabla \cdot \left(\frac{4\pi}{3\sigma_g} (1 - e^{-c\sigma_g(t-t^n)}) \nabla B_g \right) = \sigma_g (4\pi B_g - \rho_g), \quad g = 1, \dots, G, \end{aligned} \quad (2.22a)$$

$$C_v \frac{\partial T}{\partial t} = \sum_{g=1}^G \sigma_g (\rho_g - 4\pi B_g). \quad (2.22b)$$

Remark 2.1. The approximation error in (2.20) has been proved to be $O(\Delta t^2)$ for linear transport equation in [2, 41].

Remark 2.2. Our proposed model differs from UGK-type models for FRTEs [8, 45, 33]. The transport process is decomposed into two components: convection and diffusion. Specifically, the convection term involves backward tracing the microscopic perturbation $(I_g - B_g)$ along the characteristic line, while the diffusion term is obtained by approximating ∇B_g along the same characteristic line. This approach reveals that the approximation of the flux $\int_{4\pi} \boldsymbol{\Omega} I_g d\boldsymbol{\Omega}$ is not solely a function of neighboring cells, thereby eliminating the time step constraint imposed by the explicit CFL condition in the following numerical schemes.

2.3. Model correction for the semi-Lagrangian approximation

When the radiative transfer equation reduces to the gray case, the approximated macroscopic system becomes identical to the formulation presented in our previous work [1], whose effectiveness has been validated through numerical experiments. However, it is important to note that the diffusion coefficient, given by $\frac{1}{3\sigma_g}(1 - e^{-c\sigma_g(t-t^n)})$, approaches $\frac{c(t-t^n)}{3}$ rather than 0 as $\sigma_g \rightarrow 0$. This implies that the proposed model does not formally recover the free-streaming limit. While this discrepancy is generally acceptable in purely free-streaming regime (where $\nabla B_g \approx 0$), it becomes problematic at optically thick-thin interface and in frequency-dependent radiative transfer equations. To address this limitation, we introduce a model correction for our original model in the following subsection, to make it applicable also in the free streaming regime.

We introduce $\theta_g \in [0, 1]$ to give a convex combination of the time integral in (2.18):

$$\begin{aligned} I_g(\mathbf{x}, \boldsymbol{\Omega}, t) &= e^{-c\sigma_g(t-t^n)} I_g(\mathbf{X}(t^n), \boldsymbol{\Omega}, t^n) \\ &\quad + \theta_g \int_{t^n}^t e^{-c\sigma_g(t-s)} c\sigma_g B_g(\mathbf{X}(s), s) ds \\ &\quad + (1 - \theta_g) \int_{t^n}^t e^{-c\sigma_g(t-s)} c\sigma_g B_g(\mathbf{X}(s), s) ds, \end{aligned} \quad (2.23)$$

where θ_g denotes a local varying weight function associated with the opacity σ_g , characterizing the optical thickness for each group g . To capture the asymptotic behavior, we aim to keep

- $\theta_g \rightarrow 1$ in optically thin regime (relatively small σ_g),
- $\theta_g \rightarrow 0$ in optically thick regime (relatively large σ_g).

We achieve this dual asymptotic requirement through the exponential definition $\theta_g(\sigma_g, t) = e^{-c\sigma_g(t-t^n)}$ or $\theta_g(\sigma_g, t) = 1 - e^{-1/(c\sigma_g(t-t^n))}$. Numerical experiments indicate that the proposed scheme is not sensitive to the choice of the weight functions. See Section 5.3.1 for further details. In this work, we take $\theta_g(\sigma_g, t) = e^{-c\sigma_g(t-t^n)}$.

For the θ_g term in (2.23), we assume that this part represents a less stiff source, which contributes minimally in the diffusive regime. As a result, the time integral is directly approximated by

$$\begin{aligned} \theta_g \int_{t^n}^t e^{-c\sigma_g(t-s)} c\sigma_g B_g(\mathbf{X}(s), s) ds &\approx \theta_g \int_{t^n}^t c\sigma_g e^{-c\sigma_g(t-s)} ds \left(B_g(\mathbf{X}(s), s) \Big|_{s=t} \right) \\ &= \theta_g (1 - e^{-c\sigma_g(t-t^n)}) B_g(\mathbf{x}, t). \end{aligned} \quad (2.24)$$

On the other hand, for the $1 - \theta_g$ term in equation (2.23), we assume it corresponds to the stiff source, and we apply the approximation from the last subsection:

$$\begin{aligned} (1 - \theta_g) \int_{t^n}^t e^{-c\sigma_g(t-s)} c\sigma_g B_g(\mathbf{X}(s), s) ds &\approx (1 - \theta_g) \left(B_g(\mathbf{x}, t) - e^{-c\sigma_g(t-t^n)} B_g(\mathbf{X}(t^n), t^n) \right. \\ &\quad \left. - \frac{1}{c\sigma_g} (1 - e^{-c\sigma_g(t-t^n)}) \left(\frac{\partial B_g}{\partial s}(\mathbf{x}, t) + c\boldsymbol{\Omega} \cdot \nabla B_g(\mathbf{x}, t) \right) \right). \end{aligned} \quad (2.25)$$

Together, we have

$$\begin{aligned}
I_g(\mathbf{x}, \boldsymbol{\Omega}, t) &\approx e^{-c\sigma_g(t-t^n)} I_g(\mathbf{r}(t^n), \boldsymbol{\Omega}, t^n) \\
&\quad + \theta_g(1 - e^{-c\sigma_g(t-t^n)}) B_g(\mathbf{x}, t) \\
&\quad + (1 - \theta_g) \left(B_g(\mathbf{x}, t) - e^{-c\sigma_g(t-t^n)} B_g(\mathbf{X}(t^n), t^n) \right. \\
&\quad \left. - \frac{1}{c\sigma_g} (1 - e^{-c\sigma_g(t-t^n)}) \left(\frac{\partial B_g}{\partial s}(\mathbf{x}, t) + c\boldsymbol{\Omega} \cdot \nabla B_g(\mathbf{x}, t) \right) \right). \tag{2.26}
\end{aligned}$$

Similarly, substituting (2.26) into the macroscopic equation (2.15a) to close the flux $\int_{4\pi} \boldsymbol{\Omega} I_g \, d\boldsymbol{\Omega}$, it yields

$$\begin{aligned}
\frac{1}{c} \frac{\partial \rho_g}{\partial t} + \nabla \cdot \int_{4\pi} e^{-c\sigma_g(t-t^n)} \boldsymbol{\Omega} I_g(\mathbf{X}(t^n), \boldsymbol{\Omega}, t^n) \, d\boldsymbol{\Omega} \\
- \nabla \cdot \left((1 - \theta_g) \int_{4\pi} e^{-c\sigma_g(t-t^n)} \boldsymbol{\Omega} B_g(\mathbf{X}(t^n), t^n) \, d\boldsymbol{\Omega} \right) \\
- \nabla \cdot \left((1 - \theta_g) \frac{4\pi}{3\sigma_g} (1 - e^{-c\sigma_g(t-t^n)}) \nabla B_g \right) = \sigma_g (4\pi B_g - \rho_g), \quad g = 1, \dots, G, \tag{2.27a}
\end{aligned}$$

$$C_v \frac{\partial T}{\partial t} = \sum_{g=1}^G \sigma_g (\rho_g - 4\pi B_g). \tag{2.27b}$$

2.4. Reformulation

We introduce the following notations to reformulate (2.27):

$$b_g(T) := \int_{\nu_{g-\frac{1}{2}}}^{\nu_{g+\frac{1}{2}}} b(\nu, T) \, d\nu, \tag{2.28a}$$

$$\phi(T) := acT^4. \tag{2.28b}$$

From the definition of the normalized Planck function in (2.6), together with the definition of the group-wise Planck function in (2.11b), we derive the following relationship:

$$4\pi B_g = b_g \phi. \tag{2.29}$$

Applying the chain rule yields

$$\begin{aligned}
4\pi \nabla B_g &= 4\pi \frac{\partial B_g}{\partial T} \nabla T \\
&= (b_g + \frac{T}{4} \frac{\partial b_g}{\partial T}) 4acT^3 \nabla T \\
&= (b_g + \frac{T}{4} \frac{\partial b_g}{\partial T}) \nabla \phi. \tag{2.30}
\end{aligned}$$

Therefore, we can reformulate the macroscopic system (2.27) as:

$$\begin{aligned} \frac{1}{c} \frac{\partial \rho_g}{\partial t} + \nabla \cdot \int_{4\pi} e^{-c\sigma_g(t-t^n)} \boldsymbol{\Omega} I_g(\mathbf{X}(t^n), \boldsymbol{\Omega}, t^n) d\boldsymbol{\Omega} \\ - \nabla \cdot \left((1 - \theta_g) \int_{4\pi} e^{-c\sigma_g(t-t^n)} \boldsymbol{\Omega} B_g(\mathbf{X}(t^n), t^n) d\boldsymbol{\Omega} \right) \\ - \nabla \cdot \left((1 - \theta_g) \frac{1}{3\sigma_g} (1 - e^{-c\sigma_g(t-t^n)}) (b_g + \frac{T}{4} \frac{\partial b_g}{\partial T}) \nabla \phi \right) = \sigma_g (b_g \phi - \rho_g), \quad g = 1, \dots, G, \end{aligned} \quad (2.31a)$$

$$C_v \frac{\partial T}{\partial t} = \sum_{g=1}^G \sigma_g (\rho_g - b_g \phi). \quad (2.31b)$$

Remark 2.3. We use the notation $b_g \phi$ and $(b_g + \frac{T}{4} \frac{\partial b_g}{\partial T}) \nabla \phi$ to replace $4\pi B_g$ and $4\pi \nabla B_g$, respectively. This formulation offers an advantage: it enables our numerical implementation to seamlessly transition between frequency-dependent and gray radiative transfer equations. To verify this, observing that in the gray case $G = 1$, the coefficients simplify to be $b_g = 1$ and $(b_g + \frac{T}{4} \frac{\partial b_g}{\partial T}) = 1$ for all $g = 1, \dots, G$.

3. Numerical method

In this section, we present the numerical method for solving the coupled macro-micro system given by equations (2.12) and (2.31). We begin by discretizing (2.31) using a hybrid finite volume method, where the convective flux is provided by the MC method and the diffusive flux discretized implicitly with central difference. To handle the macroscopic system's nonlinearity that couples space and frequency dimensions, we employ a Picard iteration combined with a predictor-corrector approach, which decouples the system into space-only linear equations and cell-local scalar equations. The resulting material temperature T^{n+1} provides a *priori* estimate for the emission source B_g^{n+1} , thereby reducing (2.12a) to a purely absorbing radiative transport problem with a known source. This problem can be efficiently solved using the MC method.

We partition the computational domain V into N_x cells $\{V_i\}_{i=1}^{N_x}$. Let ∂V_i denote the boundary of the cell V_i , and let $S_{ij} = \partial V_i \cap \partial V_j$ denote the interface shared between the neighboring cells V_i and V_j . We denote by ΔV_i and $|S_{ij}|$ the volume of V_i and the area of S_{ij} , respectively. The set of indices of the neighboring cells of V_i that share a face is denoted by \mathcal{N}_i . Let \mathbf{n}_{ij} be the unit normal vector on S_{ij} , oriented from V_i toward V_j . Finally, let \mathbf{x}_i denote the barycenter (center of mass) of the cell V_i .

Considering a time interval $[0, T]$, we define the time step size $\Delta t = T/N_t$, where N_t is a positive integer. We then set the discrete time levels by $t^n = n\Delta t$, for $n = 1, \dots, N_t$.

3.1. A finite volume method for the macroscopic system

We integrate equation (2.31) over a time interval $[t^n, t^{n+1}]$ and a space cell V_i to obtain the following finite volume scheme:

$$\frac{\rho_{g,i}^{n+1} - \rho_{g,i}^n}{c\Delta t} + \frac{1}{\Delta V_i} \sum_{j \in \mathcal{N}_i} \left(F_{g,ij}^{C,n+1} - F_{g,ij}^{D,n+1} \right) = \sigma_{g,i}^{n+1} b_{g,i}^{n+1} \phi_i^{n+1} - \sigma_{g,i}^{n+1} \rho_{g,i}^{n+1}, \quad g = 1, \dots, G, \quad (3.1a)$$

$$C_v \frac{T_i^{n+1} - T_i^n}{\Delta t} = \sum_{g=1}^G \sigma_{g,i}^{n+1} (\rho_{g,i}^{n+1} - b_{g,i}^{n+1} \phi_i^{n+1}). \quad (3.1b)$$

The convective flux $F_{g,ij}^{C,n+1}$ is defined as:

$$F_{g,ij}^{C,n+1} = \bar{F}_{g,ij}^{I,n+1} - (1 - \theta_{g,i}^{n+1}) \bar{F}_{g,ij}^{B,n+1,+} - (1 - \theta_{g,j}^{n+1}) \bar{F}_{g,ij}^{B,n+1,-}, \quad (3.2)$$

where the weight function $\theta_{g,i}^{n+1}$ is defined implicitly as

$$\theta_{g,i}^{n+1} = e^{-c\sigma_{g,i}^{n+1}\Delta t}. \quad (3.3)$$

The component fluxes are defined as follows:

- The term $\bar{F}_{g,ij}^{I,n+1}$ denotes the surface flux contribution from the initial and boundary sources (3.28) and (3.29), defined as

$$\bar{F}_{g,ij}^{I,n+1} = \frac{1}{\Delta t} \int_{t^n}^{t^{n+1}} \int_{S_{ij}} \int_{4\pi} e^{-c\sigma_g(t-t^n)} I_g(\mathbf{X}(t^n), \Omega, t^n) \Omega \cdot \mathbf{n}_{ij} d\Omega dS dt. \quad (3.4)$$

- The term $\bar{F}_{g,ij}^{B,n+1,+}$ denotes the outflow surface flux contribution from the ghost initial and boundary sources (3.30) and (3.31), defined as

$$\bar{F}_{g,ij}^{B,n+1,+} = \frac{1}{\Delta t} \int_{t^n}^{t^{n+1}} \int_{S_{ij}} \int_{\Omega \cdot \mathbf{n}_{ij} > 0} e^{-c\sigma_g(t-t^n)} B_g(\mathbf{X}(t^n), t^n) \Omega \cdot \mathbf{n}_{ij} d\Omega dS dt. \quad (3.5)$$

- The term $\bar{F}_{g,ij}^{B,n+1,-}$ denotes the inflow surface flux contribution from the ghost initial and boundary sources (3.30) and (3.31), defined as

$$\bar{F}_{g,ij}^{B,n+1,-} = \frac{1}{\Delta t} \int_{t^n}^{t^{n+1}} \int_{S_{ij}} \int_{\Omega \cdot \mathbf{n}_{ij} < 0} e^{-c\sigma_g(t-t^n)} B_g(\mathbf{X}(t^n), t^n) \Omega \cdot \mathbf{n}_{ij} d\Omega dS dt. \quad (3.6)$$

All these integrals are evaluated using a MC solver, with details provided in (3.40) and (3.41).

The diffusive flux $F_{g,ij}^{D,n+1}$ is discretized as:

$$F_{g,ij}^{D,n+1} = D_{g,ij}^{n+1} \frac{\phi_j^{n+1} - \phi_i^{n+1}}{|\mathbf{x}_j - \mathbf{x}_i|} |S_{ij}|, \quad (3.7)$$

where the diffusion coefficient $D_{g,ij}^{n+1}$ is given by:

$$D_{g,ij}^{n+1} = (1 - \theta_{g,ij}^{n+1}) \frac{1}{3\sigma_{g,ij}^{n+1}} (1 - e^{-c\sigma_{g,ij}^{n+1}\Delta t}) (b_g + \frac{T}{4} \frac{\partial b_g}{\partial T})_{ij}^{n+1}. \quad (3.8)$$

The interface value $\theta_{g,ij}^{n+1}$ is approximated by the arithmetic average:

$$\theta_{g,ij}^{n+1} = \frac{1}{2} (\theta_{g,i}^{n+1} + \theta_{g,j}^{n+1}). \quad (3.9)$$

The interface value $\sigma_{g,ij}$ is evaluated using the harmonic average:

$$\sigma_{g,ij}^{n+1} = \frac{2\sigma_{g,i}^{n+1} \sigma_{g,j}^{n+1}}{\sigma_{g,i}^{n+1} + \sigma_{g,j}^{n+1}}. \quad (3.10)$$

Finally, the quantity $(b_g + \frac{T}{4} \frac{\partial b_g}{\partial T})_{ij}^{n+1}$ is computed based on the interface temperature T_{ij}^{n+1} , which is determined by

$$T_{ij}^{n+1} = \left(\frac{(T_i^{n+1})^4 + (T_j^{n+1})^4}{2} \right)^{\frac{1}{4}}. \quad (3.11)$$

Remark 3.1. For nonuniform cells, it is recommended to employ cell size-based weighting in the evaluation of (3.10) and (3.11). This strategy is used in the numerical tests.

Remark 3.2. We use a MC method to compute the convective flux, which, unlike the explicit deterministic methods, is not subject to the CFL constraint. In addition, the diffusion term is derived by approximating ∇B_g along the characteristic line and is discretized implicitly, thereby avoiding both the CFL and the parabolic time step restriction. These features reflect the long-range characteristic tracing inherent in our model, allowing for the use of a large time step that is independent of the speed of light.

3.1.1. Picard iteration with a predictor-corrector procedure

Directly solving the scheme (3.1) would require handling a fully coupled nonlinear system, where the coupling spans both spatial and frequency dimensions, leading to prohibitively high computational costs. To circumvent this complexity, we adopt a Picard iteration in combination with a *predictor-corrector* procedure, following the approach proposed in [9, 36].

To start with, we reformulate the system (3.1). From (3.1a), we have

$$\rho_{g,i}^{n+1} = \frac{\frac{1}{c\Delta t} \rho_{g,i}^n + \sigma_{g,i}^{n+1} b_{g,i}^{n+1} \phi_i^{n+1} - \frac{1}{\Delta V_i} \sum_{j \in \mathcal{N}_i} (F_{g,ij}^{C,n+1} - F_{g,ij}^{D,n+1})}{\frac{1}{c\Delta t} + \sigma_{g,i}^{n+1}}. \quad (3.12)$$

By substituting (3.12) into the equation (3.1b) to eliminate $\rho_{g,i}^{n+1}$, we obtain

$$C_v \frac{T_i^{n+1} - T_i^n}{\Delta t} = \sum_{g=1}^G \chi_{g,i}^{n+1} \left(\frac{1}{c\Delta t} (\rho_{g,i}^n - b_{g,i}^{n+1} \phi_i^{n+1}) - \frac{1}{\Delta V_i} \sum_{j \in \mathcal{N}_i} (F_{g,ij}^{C,n+1} - F_{g,ij}^{D,n+1}) \right), \quad (3.13)$$

where $\chi_{g,i}^{n+1} := \frac{\sigma_{g,i}^{n+1}}{\frac{1}{c\Delta t} + \sigma_{g,i}^{n+1}}$. Multiplying (2.31b) by $4acT^3$ yields

$$C_v \frac{\partial \phi}{\partial t} = 4acT^3 \sum_{g=1}^G \sigma_g (\rho_g - b_g \phi).$$

Let $\beta := \frac{4acT^3}{C_v}$, this equation can be discretized implicitly as

$$\frac{\phi_i^{n+1} - \phi_i^n}{\beta_i^{n+1} \Delta t} = \sum_{g=1}^G \sigma_{g,i}^{n+1} (\rho_{g,i}^{n+1} - b_{g,i}^{n+1} \phi_i^{n+1}). \quad (3.14)$$

By substituting (3.12) into the equation (3.14) to eliminate $\rho_{g,i}^{n+1}$, we obtain

$$\frac{\phi_i^{n+1} - \phi_i^n}{\beta_i^{n+1} \Delta t} = \sum_{g=1}^G \chi_{g,i}^{n+1} \left(\frac{1}{c\Delta t} (\rho_{g,i}^n - b_{g,i}^{n+1} \phi_i^{n+1}) - \frac{1}{\Delta V_i} \sum_{j \in \mathcal{N}_i} (F_{g,ij}^{C,n+1} - F_{g,ij}^{D,n+1}) \right). \quad (3.15)$$

Now the Picard iteration for solving (3.1) is defined as follows: for the iterative number k starting at $k = 0$, where $b_g^{n+1,0}$, $\sigma_g^{n+1,0}$, $\chi_g^{n+1,0}$ and $D_g^{n+1,0}$ can be computed by taking the value of $T^{n+1,0} = T^n$, we update the unknowns $T^{n+1,k+1}$ iteratively by the following step:

The prediction step. Using (3.15), we first solve the following *linear* system:

$$\frac{\phi_i^{n+1,k+\frac{1}{2}} - \phi_i^n}{\beta_i^{n+1,k} \Delta t} = \sum_{g=1}^G \chi_{g,i}^{n+1,k} \left(\frac{1}{c\Delta t} (\rho_{g,i}^n - b_{g,i}^{n+1,k} \phi_i^{n+1,k+\frac{1}{2}}) - \frac{1}{\Delta V_i} \sum_{j \in \mathcal{N}_i} F_{g,ij}^{n+1,k+\frac{1}{2}} \right), \quad (3.16)$$

where

$$F_{g,ij}^{n+1,k+\frac{1}{2}} = F_{g,ij}^{C,n+1,k} - F_{g,ij}^{D,n+1,k+\frac{1}{2}},$$

and

$$\begin{aligned} F_{g,ij}^{C,n+1,k} &= \bar{F}_{g,ij}^{I,n+1} - (1 - \theta_{g,i}^{n+1,k}) \bar{F}_{g,ij}^{B,n+1,+} - (1 - \theta_{g,j}^{n+1,k}) \bar{F}_{g,ij}^{B,n+1,-}, \\ F_{g,ij}^{D,n+1,k+\frac{1}{2}} &= D_{g,ij}^{n+1,k} \frac{\phi_j^{n+1,k+\frac{1}{2}} - \phi_i^{n+1,k+\frac{1}{2}}}{|\mathbf{x}_j - \mathbf{x}_i|} |S_{ij}|, \\ D_{g,ij}^{n+1,k} &= (1 - \theta_{g,ij}^{n+1,k}) \frac{1}{3\sigma_{g,ij}^{n+1,k}} (1 - e^{-c\sigma_{g,ij}^{n+1,k} \Delta t}) (b_g + \frac{T}{4} \frac{\partial b_g}{\partial T})_{ij}^{n+1,k}. \end{aligned}$$

Notice that $b_{g,i}^{n+1,k}$ and $(b_g + \frac{T}{4} \frac{\partial b_g}{\partial T})_{ij}^{n+1,k}$ are evaluated using the k th iteration values. This approach eliminates the need to solve a linear system that couples space and frequency dimensions.

To see how this forms a *linear* system, we reformulate (3.16) as follows:

$$\begin{aligned} &\left(\frac{1}{\beta_i^{n+1,k} \Delta t} + \frac{1}{c \Delta t} \sum_{g=1}^G \chi_{g,i}^{n+1,k} b_{g,i}^{n+1,k} \right) \phi_i^{n+1,k+\frac{1}{2}} \\ &- \frac{1}{\Delta V_i} \sum_{g=1}^G \chi_{g,i}^{n+1,k} \left(\sum_{j \in \mathcal{N}_i} D_{g,ij}^{n+1,k} \frac{\phi_j^{n+1,k+\frac{1}{2}} - \phi_i^{n+1,k+\frac{1}{2}}}{|\mathbf{x}_j - \mathbf{x}_i|} |S_{ij}| \right) = \text{RHS}_i, \end{aligned} \quad (3.18)$$

where

$$\text{RHS}_i = \frac{1}{\beta_i^{n+1,k} \Delta t} \phi_i^n + \sum_{g=1}^G \chi_{g,i}^{n+1,k} \left(\frac{1}{c \Delta t} \rho_{g,i}^n - \frac{1}{\Delta V_i} \sum_{j \in \mathcal{N}_i} F_{g,ij}^{C,n+1,k} \right).$$

Then at each iterative step, given $T_i^{n+1,k}$, equation (3.18) is a space-only linear system with respect to $\phi_i^{n+1,k+\frac{1}{2}}$. A standard linear solver used for solving the Poisson equation can be applied to this linear system.

The correction step. With $\phi_i^{n+1,k+\frac{1}{2}}$ obtained from the prediction step, we compute the corresponding temperature:

$$T_i^{n+1,k+\frac{1}{2}} = \left(\frac{\phi_i^{n+1,k+\frac{1}{2}}}{ac} \right)^{\frac{1}{4}},$$

which allows us to update the temperature-dependent terms $\sigma_{g,i}^{n+1,k+\frac{1}{2}}$, $\chi_{g,i}^{n+1,k+\frac{1}{2}}$, and $D_{g,ij}^{n+1,k+\frac{1}{2}}$. Using (3.13), we solve the following *scalar* nonlinear system:

$$C_v \frac{T_i^{n+1,k+1} - T_i^n}{\Delta t} = \sum_{g=1}^G \chi_{g,i}^{n+1,k+\frac{1}{2}} \left(\frac{1}{c \Delta t} \left(\rho_{g,i}^n - b_{g,i}^{n+1,k+1} \phi_i^{n+1,k+1} \right) - \frac{1}{\Delta V_i} \sum_{j \in \mathcal{N}_i} F_{g,ij}^{n+1,k+\frac{1}{2}*} \right). \quad (3.19)$$

where

$$F_{g,ij}^{n+1,k+\frac{1}{2}*} = F_{g,ij}^{C,n+1,k+\frac{1}{2}} - F_{g,ij}^{D,n+1,k+\frac{1}{2}*},$$

and

$$\begin{aligned} F_{g,ij}^{C,n+1,k+\frac{1}{2}} &= \bar{F}_{g,ij}^{I,n+1} - (1 - \theta_{g,i}^{n+1,k+\frac{1}{2}}) \bar{F}_{g,ij}^{B,n+1,+} - (1 - \theta_{g,j}^{n+1,k+\frac{1}{2}}) \bar{F}_{g,ij}^{B,n+1,-}, \\ F_{g,ij}^{D,n+1,k+\frac{1}{2}*} &= D_{g,ij}^{n+1,k+\frac{1}{2}} \frac{\phi_j^{n+1,k+\frac{1}{2}} - \phi_i^{n+1,k+\frac{1}{2}}}{|\mathbf{x}_j - \mathbf{x}_i|} |S_{ij}|, \\ D_{g,ij}^{n+1,k+\frac{1}{2}} &= (1 - \theta_{g,ij}^{n+1,k+\frac{1}{2}}) \frac{1}{3\sigma_{g,ij}^{n+1,k+\frac{1}{2}}} (1 - e^{-c\sigma_{g,ij}^{n+1,k+\frac{1}{2}} \Delta t}) (b_g + \frac{T}{4} \frac{\partial b_g}{\partial T})_{ij}^{n+1,k+\frac{1}{2}}. \end{aligned}$$

Notice that we take $(b_g + \frac{T}{4} \frac{\partial b_g}{\partial T})_{ij}^{n+1,k+\frac{1}{2}}$ to match with $\frac{\phi_j^{n+1,k+\frac{1}{2}} - \phi_i^{n+1,k+\frac{1}{2}}}{|\mathbf{x}_j - \mathbf{x}_i|}$, while $b_{g,i}^{n+1,k+1}$ matches with $\phi_i^{n+1,k+1}$. This consistent temporal treatment ensures the relation $4\pi \nabla B_g = (b_g + \frac{T}{4} \frac{\partial b_g}{\partial T}) \nabla \phi$ and $4\pi B_g = b_g \phi$ are properly maintained during the correction step. In particular, the diffusive flux $F_{g,ij}^{D,n+1,k+\frac{1}{2}*}$ is evaluated using information from the prediction step, which helps decouple the space dimension.

Utilizing $\phi_i^{n+1,k+1} = ac(T_i^{n+1,k+1})^4$, we reformulate (3.19) into the following *scalar* nonlinear system:

$$T_i^{n+1,k+1} + \frac{a}{C_v} \sum_{g=1}^G \chi_{g,i}^{n+1,k+\frac{1}{2}} b_{g,i}^{n+1,k+1} (T_i^{n+1,k+1})^4 - A_i = 0, \quad (3.21)$$

where

$$A_i = T_i^n + \frac{\Delta t}{C_v} \sum_{g=1}^G \chi_{g,i}^{n+1,k+\frac{1}{2}} \left(\frac{1}{c\Delta t} \rho_{g,i}^n - \frac{1}{\Delta V_i} \sum_{j \in \mathcal{N}_i} \left(F_{g,ij}^{C,n+1,k+\frac{1}{2}} - F_{g,ij}^{D,n+1,k+\frac{1}{2}*} \right) \right).$$

In this way, updating the temperature $T_i^{n+1,k+1}$ reduces to solving a spatially decoupled scalar nonlinear equation within each cell, thereby avoiding the need to solve a global nonlinear system across all cells. When the original equation reduces to the gray case, (3.21) simplifies to a polynomial nonlinear system, as demonstrated in [9, 36]. Here, we use Newton's iteration to solve these scalar nonlinear equations, with details provided in [Appendix A](#).

The stop criteria. The two steps are solved with the iterative number k until convergence is reached, where the stop criteria is defined as

$$\|T^{n+1,k+1} - T^{n+1,k}\|_1 < \gamma.$$

We note that, in theory, we cannot prove the convergence of the Picard iteration with (3.18) and (3.21). Nonetheless, we use the L_1 norm in our stopping criterion, and numerically all examples converge under the tolerance $\gamma = 10^{-8}$ with the maximum iterative number 50.

Remark 3.3. (Numerical boundary treatment) In our numerical tests, we consider only the isotropic boundary conditions, assuming local equilibrium at the boundary so that $I_{bc} = B(\nu, T)$. Taking 1D as an example, on the left boundary at $x_{\frac{1}{2}}$ with given T_L , the inflow boundary of I_{bc} is set as $I_{bc} = B(\nu, T_L)$, and $I_{g,bc} = b_g(T_L) \frac{ac(T_L)^4}{4\pi}$.

For the inflow part of $I_{g,\frac{1}{2}}$, we have

$$I_{g,\frac{1}{2}} = I_{g,bc}, \quad \mu > 0, \quad (3.22)$$

while for the outflow part of $I_{g,\frac{1}{2}}$, we take the approximated formal solution

$$\begin{aligned}
I_{g,\frac{1}{2}} = & e^{-c\sigma_g(t-t^n)} I_g \left(\mathbf{X}_{\frac{1}{2}}(t^n), \mu, t^n \right) \\
& + \theta_g (1 - e^{-c\sigma_g(t-t^n)}) B_g \left(x_{\frac{1}{2}}, t \right) \\
& + (1 - \theta_g) \left[B_g \left(x_{\frac{1}{2}}, t \right) - B_g \left(\mathbf{X}_{\frac{1}{2}}(t^n), t^n \right) e^{-c\sigma_g(t-t^n)} \right. \\
& \quad \left. - \frac{1}{c\sigma_g} (1 - e^{-c\sigma_g(t-t^n)}) \left(\frac{\partial B_g}{\partial t}(x_{\frac{1}{2}}, t) + c\mu \frac{\partial B_g}{\partial x}(x_{\frac{1}{2}}, t) \right) \right], \quad \mu < 0.
\end{aligned} \tag{3.23}$$

We set $\theta_{g,\frac{1}{2}} = \theta_{g,1}$, $\sigma_{g,\frac{1}{2}} = \sigma_{g,1}$, and define $\phi_{\frac{1}{2}} = \frac{1}{2}(4\pi I_{bc} + \phi_1^n)$. The temperature $T_{\frac{1}{2}}$ is then computed as $T_{\frac{1}{2}} = \left(\frac{\phi_{\frac{1}{2}}}{ac} \right)^{\frac{1}{4}}$, which is subsequently used to evaluate both $b_{g,\frac{1}{2}}$ and $\left(b_g + \frac{T}{4} \frac{\partial b_g}{\partial T} \right)_{\frac{1}{2}}$. Substituting (3.23) into $\langle \mu I_{g,\frac{1}{2}} \rangle$, where $\langle \cdot \rangle := 2\pi \int_{-1}^1 d\mu$, and applying numerical discretization, we obtain:

$$\begin{aligned}
\langle \mu I_{g,\frac{1}{2}} \rangle = & I_{g,bc} \langle \mu \mathbf{1}_{\mu>0} \rangle + (1 - \theta_{g,\frac{1}{2}} e^{-c\sigma_{g,\frac{1}{2}}(t-t^n)}) b_{g,\frac{1}{2}} \phi_{\frac{1}{2}} \langle \mu \mathbf{1}_{\mu<0} \rangle \\
& + \langle \mu e^{-c\sigma_{g,\frac{1}{2}}(t-t^n)} I_g \left(\mathbf{X}_{\frac{1}{2}}(t^n), \mu, t^n \right) \mathbf{1}_{\mu<0} \rangle \\
& - (1 - \theta_{g,\frac{1}{2}}) \langle \mu e^{-c\sigma_{g,\frac{1}{2}}(t-t^n)} B_g \left(\mathbf{X}_{\frac{1}{2}}(t^n), t^n \right) \mathbf{1}_{\mu<0} \rangle \\
& - (1 - \theta_{g,\frac{1}{2}}) \frac{\langle \mu^2 \mathbf{1}_{\mu<0} \rangle}{4\pi\sigma_{g,\frac{1}{2}}} (1 - e^{-c\sigma_{g,\frac{1}{2}}(t-t^n)}) (b_g + \frac{T}{4} \frac{\partial b_g}{\partial T})_{\frac{1}{2}} \frac{\phi_{\frac{1}{2}} - \phi_1}{\Delta x_1/2},
\end{aligned} \tag{3.24}$$

where the directional indicator function $\mathbf{1}_{\mu \leq 0}$ takes value 1 when $\mu \leq 0$ and 0 otherwise. Here, we have $\langle \mu \mathbf{1}_{\mu<0} \rangle = -\pi$, $\langle \mu \mathbf{1}_{\mu>0} \rangle = \pi$ and $\langle \mu^2 \mathbf{1}_{\mu<0} \rangle = \frac{4\pi}{6}$.

A similar approach is applied for vacuum boundary condition, and the formulation can be naturally extended to two-dimensional cases along each direction.

3.2. A Monte Carlo method for the microscopic system

In this subsection, we present a particle-based MC method for solving the microscopic transport equation. The microscopic evolution also yields the convective flux $F_{g,ij}^{C,n+1}$, which is used to in the finite volume scheme (3.1). Since the emission source $B_{g,i}^{n+1}$ can be determined by the material temperature T_i^{n+1} from the macroscopic system, the microscopic equation (2.12a) reduces to a purely absorbing problem. A MC method for (2.12a) is thus straightforward. Finally, to ensure consistency, the final material temperatures T_i^{n+1} are updated by tallying the results from the MC solution of the microscopic transport equation, rather than using the values from the macroscopic system.

Due to Duhamel's principle, in each time interval $[t^n, t^{n+1}]$, the microscopic equation (2.12a) can be divided into the following two subsystems:

$$\begin{cases} \frac{1}{c} \frac{\partial I_{1,g}}{\partial t} + \boldsymbol{\Omega} \cdot \nabla I_{1,g} + \sigma_g I_{1,g} = 0, \\ I_{1,g}(\mathbf{x}, \boldsymbol{\Omega}, t^n) = I_g^n(\mathbf{x}, \boldsymbol{\Omega}), \\ I_{1,g}(\mathbf{x}, \boldsymbol{\Omega}, t) \big|_{\mathbf{x} \in \partial V} = I_{bc,g}(\mathbf{x}, \boldsymbol{\Omega}, t), \quad \boldsymbol{\Omega} \cdot \mathbf{n} < 0, \end{cases} \tag{3.25}$$

and

$$\begin{cases} \frac{1}{c} \frac{\partial I_{2,g}}{\partial t} + \boldsymbol{\Omega} \cdot \nabla I_{2,g} + \sigma_g I_{2,g} = \sigma_g B_g, \\ I_{2,g}(\mathbf{x}, \boldsymbol{\Omega}, t^n) = 0, \\ I_{2,g}(\mathbf{x}, \boldsymbol{\Omega}, t) \Big|_{\mathbf{x} \in \partial V} = 0, \quad \boldsymbol{\Omega} \cdot \mathbf{n} < 0. \end{cases} \quad (3.26)$$

Here I_g^n and $I_{bc,g}$ represent the group-wise radiation intensity at time t^n and on the boundary, respectively. Systems (3.25) and (3.26) indicate that the total intensity originates from two distinct sources. The first source consists of photons from the previous time step (or initial condition) and the boundary, which are already known and can be tracked immediately. The second source corresponds to the unknown photons emitted by the material, which can be calculated with T^{n+1} from the macroscopic equation.

In a particle based method, the group-wise radiation intensity I_g is represented as a collection of particles, and can be expressed as

$$I_g(\mathbf{x}, \boldsymbol{\Omega}, t) = \sum_{p=1}^{N(t)} c \omega_p^g(t) \delta(\mathbf{x} - \mathbf{x}_p(t)) \delta(\boldsymbol{\Omega} - \boldsymbol{\Omega}_p(t)), \quad (3.27)$$

where $\mathbf{x}_p(t)$, $\boldsymbol{\Omega}_p(t)$ and $\omega_p^g(t)$ are the location, angular direction and group-wise energy weight of particle p at time t , respectively. $N(t)$ is the total number of MC particles used at time t .

The essence of the particle based MC method lies in the fact that each particle is represented as a quadruple $(\mathbf{x}_p, \boldsymbol{\Omega}_p, \omega_p^g, t_p)$, which is used to mimic the transport and absorption behavior. We can then recover the necessary physical quantities (related to the solution of the original PDE) from these ensembles of particles.

3.2.1. Particle sampling

To solve systems (3.25) and (3.26), one needs to sample MC particles from the previous time step (or the initial condition), the boundary condition and the emission source. Each particle is assigned a position, angular direction, time, and energy weight. Details on how to sample position, angular direction, and time can be found in [11, 46]. Here, we focus on the way to compute the corresponding energy and assign energy weights to ensure energy conservation.

For particles from the initial condition or the previous time step, the function I_g^n is employed for sampling the position and angular direction of a particle. The radiation energy for this portion of particles can be obtained by integrating the radiation intensity I_g^n over the cell and angle

$$E_{g,i}^{I,n} = \frac{1}{c} \int_{V_i} \int_{4\pi} I_g^n(\mathbf{x}, \boldsymbol{\Omega}) d\boldsymbol{\Omega} d\mathbf{x}. \quad (3.28)$$

Similarly, The total energy due to the boundary condition is obtained by integrating the function $I_{bc,g}$ over the time step, boundary surface, and angle corresponding to an inflow part

$$E_g^{I,bc} = \int_{t^n}^{t^{n+1}} \int_{\boldsymbol{\Omega} \cdot \mathbf{n} < 0} \int_{\partial V} (-\boldsymbol{\Omega} \cdot \mathbf{n}) I_{bc,g}(\mathbf{x}, \boldsymbol{\Omega}, t) dS d\boldsymbol{\Omega} dt. \quad (3.29)$$

However, the boundary source is frequently specified as a Planck function at a fixed temperature, i.e., $I_{bc,g}(\mathbf{x}, \boldsymbol{\Omega}, t) = B_g(T_{bc}(\mathbf{x}))$, in which case the total energy may be written more simply as

$$E_g^{I,bc} = \pi \Delta t \int_{\partial V} B_g(T_{bc}(\mathbf{x})) dS.$$

As noted from the last subsection, the convective flux $F_{ij}^{C,n+1}$, given by

$$F_{g,ij}^{C,n+1} = \bar{F}_{g,ij}^{I,n+1} - (1 - \theta_{g,i}^{n+1}) \bar{F}_{g,ij}^{B,n+1,+} - (1 - \theta_{g,j}^{n+1}) \bar{F}_{g,ij}^{B,n+1,-},$$

is obtained by the MC solver. Those photons from the source (3.28) and (3.29) contributes to the first term $\bar{F}_{g,ij}^{I,n+1}$. While for $\bar{F}_{g,ij}^{B,n+1,+}$ and $\bar{F}_{g,ij}^{B,n+1,-}$, these photons can be calculated similarly, given by the ghost sources

$$E_{g,i}^{B,n} = \frac{1}{c} \int_{V_i} \int_{4\pi} B_g^n(\mathbf{x}) d\Omega d\mathbf{x}, \quad (3.30)$$

and

$$E_g^{B,bc} = \int_{t^n}^{t^{n+1}} \int_{\Omega \cdot \mathbf{n} < 0} \int_{\partial V} (-\Omega \cdot \mathbf{n}) B_{bc,g}^n(\mathbf{x}) dS d\Omega dt. \quad (3.31)$$

The definition of $B_{bc,g}^n(\mathbf{x})$ is consistent with the boundary treatment for the macroscopic equation. In 1D example, $B_{bc,g}^n(\mathbf{x})$ corresponds specifically to the term $b_{g,\frac{1}{2}} \phi_{\frac{1}{2}}$ defined in the first line of equation (3.24). We emphasize that photons from ghost sources are used exclusively for tallying the convective flux $F_{ij}^{C,n+1}$ —they neither enter the census¹ nor contribute to absorption energy calculations.

Next, we consider the MC particles emitted from the material. For these particles, the radiation energy is computed from the macroscopic variables, which is

$$E_{g,i}^{R,n+1} = \int_{t_n}^{t^{n+1}} \int_{V_i} \int_{4\pi} \sigma_g^{n+1} B_g^{n+1} d\Omega d\mathbf{x} dt = 4\pi \sigma_{g,i}^{n+1} B_{g,i}^{n+1} \Delta V_i \Delta t, \quad (3.32)$$

where $B_{g,i}^{n+1}$ is the cell average evaluated using T_i^{n+1} from the macroscopic equations. As shown in [12, 42, 47], in order to capture the asymptotic diffusion limit of the radiative transfer equations, a linear representation of the emission source is necessary. In the following, we will present a continuous *source tilting* method for the emission source, extending our previous work [42] for the frequency dependent radiative transfer equation.

We consider the 1D case for illustration, while the extension to 2D is available in [42]. In 1D, for each cell V_i centered at x_i with mesh size Δx_i , we define the linear reconstruction of $(B_{tilt})_{g,i}^{n+1}$ as

$$(B_{tilt})_{g,i}^{n+1}(x) = B_{g,i}^{n+1} + \begin{cases} s_{g,i}^B(x - x_i), & \text{if } \mu < 0, \\ s_{g,i}^F(x - x_i), & \text{if } \mu > 0, \end{cases} \quad (3.33)$$

where $B_{g,i}^{n+1}$ is the cell average. The backward and forward one-sided slopes are given by

$$s_{g,i}^B = \frac{B_{g,i}^{n+1} - B_{g,i-1}^{n+1}}{\frac{1}{2}(\Delta x_i + \Delta x_{i-1})}, \quad s_{g,i}^F = \frac{B_{g,i+1}^{n+1} - B_{g,i}^{n+1}}{\frac{1}{2}(\Delta x_{i+1} + \Delta x_i)}.$$

With this definition, the particle positions drawn from the emission source in cell V_i follow the probability distribution function

$$p_g(x) \Big|_{V_i} = \frac{1}{\Delta x_i} \frac{(B_{tilt})_{g,i}^{n+1}(x)}{B_{g,i}^{n+1}}. \quad (3.34)$$

¹In radiative transfer terminology, this typically refers to particles advancing to the next time step.

To ensure positivity of the probability distribution function, the slopes must satisfy [47]

$$|s_{g,i}^B| \leq \frac{2B_{g,i}^{n+1}}{\Delta x_i}, \quad |s_{g,i}^F| \leq \frac{2B_{g,i}^{n+1}}{\Delta x_i}.$$

We remark that equation (3.33) is used to bias the distribution of the locations for the emission photons via (3.34) (replacing uniform sampling in V_i), while the total emission source strength (3.32) remains determined directly by the cell-averaged values $B_{g,i}^{n+1}$.

3.2.2. Particle tracking

After all MC particles have been sampled, the subsequent task involves tracking each particle's trajectory. As previously noted, the system transitions to a purely absorbing scenario once the emission source is established, simplifying the tracking process. Three fundamental events govern particle trajectories: (i) absorption by material, (ii) traversal across a cell interface, or (iii) survival until reaching the end of the time step at t^{n+1} . Each event corresponds to a distinct characteristic distance: the absorption distance d_A , the boundary distance d_B to the cell interface, and the temporal survival distance d_T . The distance to the cell interface d_B satisfies

$$\mathbf{x}_B - \mathbf{x}_p = d_B \boldsymbol{\Omega}_p,$$

where \mathbf{x}_p is the location of particle p , \mathbf{x}_B is the cell interface location in direction $\boldsymbol{\Omega}_p$. The temporal survival distance d_T is

$$d_T = c(t^{n+1} - t),$$

where t is the current time of each particle and c is the speed of light. For the absorption event, we employ the *continuous energy deposition* variance reduction technique [11]. In this approach, the absorption distance d_A is implicitly determined through exponential decay of the energy weight rather than explicit calculation. In summary, if we let

$$d = \min(d_B, d_T),$$

the particle p is advanced according to

$$\begin{aligned} \mathbf{x}'_p &= \mathbf{x}_p + \boldsymbol{\Omega}_p d, \\ \boldsymbol{\Omega}'_p &= \boldsymbol{\Omega}_p, \\ t' &= t + d/c, \\ \omega_p^{g'} &= \omega_p^g e^{-\sigma_g d}, \end{aligned}$$

where \mathbf{x}'_p , $\boldsymbol{\Omega}'_p$, t' and $\omega_p^{g'}$ denote the new location, direction, time and group-wise energy weight of each particle, respectively. Thanks to d_B , we partition the tracking step for each spatial cell, where the group-wise absorption opacity σ_g is assumed to be constant.

The tracking process for each particle continues until one of three termination conditions is met: (i) the particle's current energy weight falls below 0.01% of its initial birth weight, (ii) the particle leaks out of the physical domain V , or (iii) the particle enters census.

3.2.3. Tally

During the evolution of particle trajectory, the following three quantities need to be tallied.

- The first quantity is the amount of radiation energy at the new time step in each cell. This value can be evaluated by

$$E_{g,i}^{I,n+1} = \sum_{p=1}^M \omega_p^g(t^{n+1}), \quad (3.35)$$

where $p = 1, 2, \dots, M$ denote the number of particles that go to census in the cell V_i . We note that only the particles from the radiation sources (3.28) (3.29) and (3.32) are used for tallying of this quantity. The group-wise angular integrated intensity at the new time step can then be calculated by

$$\rho_{g,i}^{n+1} = \frac{cE_{g,i}^{I,n+1}}{\Delta V_i}. \quad (3.36)$$

Additionally, we use this quantity to compute the radiation temperature:

$$T_{r,i}^{n+1} = \left(\frac{\sum_{g=1}^G E_{g,i}^{I,n+1}}{a \Delta V_i} \right)^{\frac{1}{4}}. \quad (3.37)$$

- The second quantity is the radiation energy deposited due to absorption in each cell in $[t^n, t^{n+1}]$, which is given by

$$E_{g,i}^{A,n+1} := \frac{1}{c} \int_{t^n}^{t^{n+1}} \int_{V_i} \int_{4\pi} c \sigma_g I_g d\Omega dx dt = \sum_{p=1}^N \omega_p^g (1 - e^{-\sigma_{g,i} d}), \quad (3.38)$$

where $p = 1, 2, \dots, N$ denote the number of particles traversing cell V_i during the time interval $[t^n, t^{n+1}]$, and d represents the traveling distance within V_i over $[t^n, t^{n+1}]$. We emphasize that only particles originating from the sources in (3.28), (3.29), and (3.32) are considered for tallying this quantity. This value is used in updating the material temperature T_i^{n+1} by integrating equation (2.12b) over V_i and $[t^n, t^{n+1}]$:

$$T_i^{n+1} = T_i^n + \frac{1}{C_v} \frac{1}{\Delta V_i} \sum_{g=1}^G (E_{g,i}^{A,n+1} - E_{g,i}^{R,n+1}). \quad (3.39)$$

To ensure consistency, T_i^{n+1} is updated for the next time step using (3.39), rather than adopting the quantities from the macroscopic system.

- The final quantities to be computed are the net particle fluxes across the surface S_{ij} during the time interval $[t^n, t^{n+1}]$. They are computed by

$$\bar{F}_{g,ij}^{I,n+1} = \frac{1}{\Delta t} \sum_{p=1}^K \text{sign}(\boldsymbol{\Omega} \cdot \mathbf{n}_{ij}) \omega_p^g, \quad (3.40)$$

where $p = 1, 2, \dots, K$ denote the numbers of particles originated from the sources (3.28) and (3.29) that traverse the interface S_{ij} during $[t^n, t^{n+1}]$. And

$$\begin{aligned} \bar{F}_{g,ij}^{B,n+1,+} &= \frac{1}{\Delta t} \sum_{p=1}^L \text{sign}(\boldsymbol{\Omega} \cdot \mathbf{n}_{i,j}) \omega_p^g \mathbf{1}_{\boldsymbol{\Omega} \cdot \mathbf{n}_{ij} > 0}, \\ \bar{F}_{g,ij}^{B,n+1,-} &= \frac{1}{\Delta t} \sum_{p=1}^L \text{sign}(\boldsymbol{\Omega} \cdot \mathbf{n}_{i,j}) \omega_p^g \mathbf{1}_{\boldsymbol{\Omega} \cdot \mathbf{n}_{ij} < 0}, \end{aligned} \quad (3.41)$$

where $p = 1, 2, \dots, L$ denote the numbers of particles originated from the ghost sources (3.30) and (3.31) that traverse the interface S_{ij} during $[t^n, t^{n+1}]$.

3.3. An overall algorithm

Finally we present our updating procedure from t^n to t^{n+1} in Algorithm (3.1).

Algorithm 3.1 The updating procedure from t^n to t^{n+1} .

- 1: Evaluate multi-group opacity $\sigma_g(T_i^n)$;
- 2: Sample MC particles from radiation sources $E_{g,i}^{I,n}$, $E_g^{I,bc}$, $E_{g,i}^{B,n}$, $E_g^{B,bc}$;
- 3: Track particle trajectories,
 - For particles from $E_{g,i}^{I,n}$, $E_g^{I,bc}$, tally the convective flux $\bar{F}_{g,ij}^{I,n+1}$, the radiation energy $E_{g,i}^{I,n+1}$, and the absorbed energy $E_{g,i}^{A,n+1}$; this resolves (3.25);
 - For particles from $E_{g,i}^{B,n}$, $E_g^{B,bc}$, tally only the convective flux $\bar{F}_{g,ij}^{B,n+1,+}$ and $\bar{F}_{g,ij}^{B,n+1,-}$;
- 4: Solve the macroscopic system (3.1) to obtain T_i^{n+1} , and update $B_{g,i}^{n+1}$ accordingly;
- 5: Evaluate multi-group opacity $\sigma_g(T_i^{n+1})$;
- 6: Reconstruct linear source term $(B_{tilt})_{g,i}^{n+1}$;
- 7: Sample MC particles from the emission source $E_{g,i}^{R,n+1}$;
- 8: Track particle trajectories from $E_{g,i}^{R,n+1}$, tally the radiation energy $E_{g,i}^{I,n+1}$, and the absorbed energy $E_{g,i}^{A,n+1}$; this resolves (3.26);
- 9: Update group-wise angular integrated intensity $\rho_{g,i}^{n+1}$ and material temperatures T_i^{n+1} using (3.36) and (3.39), respectively.

4. Formal asymptotic analysis

In this section, we will formally prove the proposed numerical method preserves the asymptotic property in the equilibrium diffusion limit.

Let $\varepsilon > 0$ denote the dimensionless Knudsen number, defined as the ratio of the mean free path to the characteristic length scale of the system. If the system is optically thick, and the speed of light is fast compared to the time evolution of I , then the radiative transfer equations (2.1) can be rewritten in the following scaled form [43]:

$$\begin{aligned} \frac{\varepsilon^2}{c} \frac{\partial I}{\partial t} + \varepsilon \boldsymbol{\Omega} \cdot \nabla I &= \sigma(B - I), \\ \varepsilon^2 C_v \frac{\partial T}{\partial t} &= \int_0^\infty \int_{4\pi} \sigma(I - B) d\boldsymbol{\Omega} d\nu, \end{aligned} \tag{4.1}$$

where the opacity, heat capacity, and speed of light are scaled as

$$\sigma \rightarrow \frac{\sigma}{\varepsilon}, \quad c \rightarrow \frac{c}{\varepsilon}, \quad C_v \rightarrow \varepsilon C_v, \tag{4.2}$$

respectively. We note that the scale of c does not apply to the emission source term because this term is a Planckian at the local material temperature, which does not change in the equilibrium diffusion limit. In [25, 48], Larsen et al. have shown that away from boundaries and initial

times, as $\varepsilon \rightarrow 0$, the leading order radiation intensity $I^{(0)}$ approaches to a Planckian at the local temperature,

$$I^{(0)} = B(\nu, T^{(0)}), \quad (4.3)$$

and the leading order material temperature $T^{(0)}$ satisfies the following radiation diffusion equation

$$a \frac{\partial}{\partial t} (T^{(0)})^4 + C_v \frac{\partial}{\partial t} T^{(0)} = \nabla \cdot \left(\frac{ac}{3\sigma_R} \nabla (T^{(0)})^4 \right), \quad (4.4)$$

with the Rosseland mean opacity σ_R given by

$$\frac{1}{\sigma_R} = \frac{\int_0^\infty \frac{1}{\sigma} \frac{\partial B(\nu, T^{(0)})}{\partial T} d\nu}{\int_0^\infty \frac{\partial B(\nu, T^{(0)})}{\partial T} d\nu}. \quad (4.5)$$

Next, We will analyze the asymptotic behavior of the proposed method by expanding the group-integrated radiation intensity and the material temperature in powers of ε :

$$I_g = \sum_{k=0}^{\infty} \varepsilon^k I_g^{(k)}, \quad (4.6)$$

and

$$T = \sum_{k=0}^{\infty} \varepsilon^k T^{(k)}, \quad (4.7)$$

and compare terms that are the same order in ε . The temperature-dependent terms can also be expanded into a power series in ε . For example, the group integrated Planck function $B_g(T)$ can be written as

$$B_g = B_g^{(0)} + \varepsilon B_g^{(1)} + \dots, \quad (4.8)$$

where

$$\begin{aligned} B_g^{(0)} &= B_g|_{\varepsilon=0} = B_g|_{T=T^{(0)}}, \\ B_g^{(1)} &= \frac{\partial B_g}{\partial \varepsilon} \Big|_{\varepsilon=0} = \frac{\partial B_g}{\partial T} \frac{\partial T}{\partial \varepsilon} \Big|_{\varepsilon=0} = \frac{\partial B_g}{\partial T} \Big|_{T=T^{(0)}} T^{(1)}. \end{aligned}$$

We first show the multi-group discretization using piecewise constant approximation is asymptotic preserving, this proposition comes from [2].

Proposition 4.1. *When ε tends to 0, the limit of the multi-group discretization of the scaled radiative transfer equation (4.1) utilizing piecewise constant approximation (2.13) approaches to the radiation diffusion equation (4.4).*

Proof. Consider the systems

$$\frac{\varepsilon^2}{c} \frac{\partial I_g}{\partial t} + \varepsilon \boldsymbol{\Omega} \cdot \nabla I_g = \sigma_g B_g - \sigma_g I_g, \quad g = 1, \dots, G, \quad (4.9a)$$

$$\varepsilon^2 C_v \frac{\partial T}{\partial t} = \sum_{g=1}^G \sigma_g (\rho_g - 4\pi B_g). \quad (4.9b)$$

We now perform a Chapman-Enskog expansion and compare terms that are the same order in ε .

The $O(1)$ equation for (4.9a) is

$$I_g^{(0)} = B_g^{(0)}, \quad g = 1, \dots, G, \quad (4.10)$$

integrating (4.10) over the angular variables, we have

$$\rho_g^{(0)} = 4\pi B_g^{(0)}, \quad g = 1, \dots, G. \quad (4.11)$$

The $O(\varepsilon)$ equation for (4.9a) is

$$\boldsymbol{\Omega} \cdot \nabla I_g^{(0)} + \sigma_g I_g^{(1)} = \sigma_g B_g^{(1)}, \quad g = 1, \dots, G, \quad (4.12)$$

substituting (4.10) into (4.12), we can get

$$I_g^{(1)} = -\frac{1}{\sigma_g} \boldsymbol{\Omega} \cdot \nabla B_g^{(0)} + B_g^{(1)}, \quad g = 1, \dots, G. \quad (4.13)$$

The $O(\varepsilon^2)$ equation for (4.9a) is

$$\frac{1}{c} \frac{\partial I_g^{(0)}}{\partial t} + \boldsymbol{\Omega} \cdot \nabla I_g^{(1)} = \sigma_g B_g^{(2)} - \sigma_g I_g^{(2)}, \quad g = 1, \dots, G, \quad (4.14)$$

The $O(\varepsilon^2)$ equation for (4.9b) is

$$C_v \frac{\partial}{\partial t} T^{(0)} = \sum_{g=1}^G \sigma_g (\rho_g^{(2)} - 4\pi B_g^{(2)}). \quad (4.15)$$

Integrating (4.14) over the angular variables, adding up all groups and using (4.15), we have

$$\frac{1}{c} \frac{\partial}{\partial t} \left(\sum_{g=1}^G \rho_g^{(0)} \right) + C_v \frac{\partial}{\partial t} T^{(0)} = - \sum_{g=1}^G \nabla \cdot \int_{4\pi} \boldsymbol{\Omega} I_g^{(1)} d\Omega. \quad (4.16)$$

Plugging (4.13) into the equation (4.16), using the condition (4.11), then (4.16) reduces to

$$\frac{1}{c} \frac{\partial}{\partial t} \left(4\pi \sum_{g=1}^G B_g^{(0)} \right) + C_v \frac{\partial}{\partial t} T^{(0)} = \sum_{g=1}^G \nabla \cdot \left(\frac{4\pi}{3\sigma_g} \nabla B_g^{(0)} \right), \quad (4.17)$$

which implies that (by chain rules)

$$\frac{1}{c} \frac{\partial}{\partial t} \left(4\pi \sum_{g=1}^G B_g^{(0)} \right) + C_v \frac{\partial}{\partial t} T^{(0)} = \sum_{g=1}^G \nabla \cdot \left(\frac{ac}{3\sigma_g} \frac{\partial B_g^{(0)}}{\partial T} \frac{4\pi}{4ac(T^{(0)})^3} \nabla (T^{(0)})^4 \right). \quad (4.18)$$

Using the following relations

$$4\pi \sum_{g=1}^G B_g = acT^4, \quad 4\pi \sum_{g=1}^G \frac{\partial B_g}{\partial T} = 4acT^3,$$

(4.18) reduces to

$$a \frac{\partial}{\partial t} (T^{(0)})^4 + C_v \frac{\partial}{\partial t} T^{(0)} = \nabla \cdot \left(\frac{ac}{3\hat{\sigma}_R} \nabla (T^{(0)})^4 \right), \quad (4.19)$$

where the mean opacity $\hat{\sigma}_R$ is defined by

$$\frac{1}{\hat{\sigma}_R} = \frac{1}{\sum_{g=1}^G \frac{\partial B_g^{(0)}}{\partial T}} \left(\sum_{g=1}^G \frac{1}{\sigma_g} \frac{\partial B_g^{(0)}}{\partial T} \right). \quad (4.20)$$

When one approximates σ_g as in (2.13), i.e.,

$$\sigma_g = \frac{1}{\nu_{g+\frac{1}{2}} - \nu_{g-\frac{1}{2}}} \int_{\nu_{g-\frac{1}{2}}}^{\nu_{g+\frac{1}{2}}} \sigma d\nu,$$

the approximated mean opacity $\hat{\sigma}_R$ of the above equation is determined by

$$\frac{1}{\hat{\sigma}_R} = \frac{1}{\sum_{g=1}^G \int_{\nu_{g-\frac{1}{2}}}^{\nu_{g+\frac{1}{2}}} \frac{1}{\partial B(\nu, T^{(0)})} d\nu} \left(\sum_{g=1}^G \frac{1}{\frac{1}{\nu_{g+\frac{1}{2}} - \nu_{g-\frac{1}{2}}} \int_{\nu_{g-\frac{1}{2}}}^{\nu_{g+\frac{1}{2}}} \sigma d\nu} \int_{\nu_{g-\frac{1}{2}}}^{\nu_{g+\frac{1}{2}}} \frac{\partial B(\nu, T^{(0)})}{\partial T} d\nu \right), \quad (4.21)$$

which is indeed a reasonable approximation for (4.5). \square

We now state a useful lemma.

Lemma 4.2. *When ε tends to 0, we have:*

- $\theta_{g,i}^{n+1} = e^{-c\sigma_i^{n+1}\Delta t/\varepsilon^2} \rightarrow 0$,
- $\theta_{g,ij}^{n+1} = \frac{1}{2}(\theta_{g,i}^{n+1} + \theta_{g,j}^{n+1}) \rightarrow 0$,
- $D_{g,ij}^{n+1} = (1 - \theta_{g,ij}^{n+1}) \frac{\varepsilon}{3\sigma_{g,ij}^{n+1}} (1 - e^{-c\sigma_{g,ij}^{n+1}\Delta t/\varepsilon^2}) (b_g + \frac{T}{4} \frac{\partial b_g}{\partial T})_{ij}^{n+1} \rightarrow \frac{\varepsilon}{3\sigma_{g,ij}^{n+1}} (b_g + \frac{T}{4} \frac{\partial b_g}{\partial T})_{ij}^{n+1}$,
- $\chi_{g,i}^{n+1} = \frac{\sigma_{g,i}^{n+1}}{\frac{\varepsilon^2}{c\Delta t} + \sigma_{g,i}^{n+1}} \rightarrow 1$.

As a consequence, the convective flux $F_{g,ij}^{C,n+1}$ defined in (3.2) has the following limit:

$$F_{g,ij}^{C,n+1} = \bar{F}_{g,ij}^{I,n+1} - (1 - \theta_{g,i}^{n+1,k}) \bar{F}_{g,ij}^{B,n+1,+} - (1 - \theta_{g,j}^{n+1,k}) \bar{F}_{g,ij}^{B,n+1,-} \xrightarrow[\varepsilon \rightarrow 0]{} 0,$$

while the diffusive flux $F_{g,ij}^{D,n+1}$ defined in (3.7) scaled by the factor $\frac{1}{\varepsilon}$ has the following limit:

$$\frac{1}{\varepsilon} F_{g,ij}^{D,n+1} = \frac{1}{\varepsilon} D_{g,ij}^{n+1} \frac{\phi_j^{n+1} - \phi_i^{n+1}}{|\mathbf{x}_j - \mathbf{x}_i|} |S_{ij}| \xrightarrow[\varepsilon \rightarrow 0]{} \frac{1}{3\sigma_{g,ij}^{n+1}} (b_g + \frac{T}{4} \frac{\partial b_g}{\partial T})_{ij}^{n+1} \frac{\phi_j^{n+1} - \phi_i^{n+1}}{|\mathbf{x}_j - \mathbf{x}_i|} |S_{ij}|.$$

Next, we show that the full discretization with Picard iteration with predictor-corrector procedure possesses the following asymptotic behavior.

Proposition 4.3. *When ε tends to 0, in the prediction step, the limit of the full discretization of the scaled radiative transfer equation (4.1) approaches to the implicit scheme for the quasilinear diffusion equation for $(T^{(0)})^4$:*

$$\left(\frac{C_v}{4(T^{(0)})^3} + a \right) \frac{\partial}{\partial t} (T^{(0)})^4 = \nabla \cdot \left(\frac{ac}{3\sigma_R} \nabla (T^{(0)})^4 \right), \quad (4.22)$$

while in the correction step, the limit approaches to the implicit scheme for the nonlinear diffusion equation for $T^{(0)}$:

$$a \frac{\partial}{\partial t} (T^{(0)})^4 + C_v \frac{\partial}{\partial t} T^{(0)} = \nabla \cdot \left(\frac{ac}{3\sigma_R} \nabla (T^{(0)})^4 \right). \quad (4.23)$$

Proof. In the prediction step (3.18), with the scale (4.2), we have the scheme:

$$\begin{aligned} & \left(\frac{1}{\beta_i^{n+1,k} \Delta t} + \frac{1}{c \Delta t} \sum_{g=1}^G \chi_{g,i}^{n+1,k} b_{g,i}^{n+1,k} \right) \phi_i^{n+1,k+\frac{1}{2}} \\ & - \frac{1}{\varepsilon \Delta V_i} \sum_{g=1}^G \chi_{g,i}^{n+1,k} \left(\sum_{j \in \mathcal{N}_i} D_{g,ij}^{n+1,k} \frac{\phi_j^{n+1,k+\frac{1}{2}} - \phi_i^{n+1,k+\frac{1}{2}}}{|\mathbf{x}_j - \mathbf{x}_i|} |S_{ij}| \right) = \text{RHS}_1, \end{aligned} \quad (4.24)$$

where

$$\text{RHS}_1 = \frac{1}{\beta_i^{n+1,k} \Delta t} \phi_i^n + \sum_{g=1}^G \chi_{g,i}^{n+1,k} \left(\frac{1}{c \Delta t} \rho_{g,i}^n - \frac{1}{\varepsilon \Delta V_i} \sum_{j \in \mathcal{N}_i} F_{g,ij}^{C,n+1,k} \right).$$

In the limit $\varepsilon \rightarrow 0$ with Chapman-Enskog expansion, using the lemma above, the system reduces to:

$$\begin{aligned} & \frac{1}{\beta_i^{n+1,k,(0)} \Delta t} (\phi_i^{n+1,k+\frac{1}{2},(0)} - \phi_i^{n,(0)}) + \frac{1}{c \Delta t} \sum_{g=1}^G \left(b_{g,i}^{n+1,k,(0)} \phi_i^{n+1,k+\frac{1}{2},(0)} - \rho_{g,i}^{n,(0)} \right) \\ & = \frac{1}{\Delta V_i} \sum_{j \in \mathcal{N}_i} \left(\sum_{g=1}^G \frac{1}{3\sigma_{g,ij}^{n+1,k,(0)}} \left(b_g + \frac{T}{4} \frac{\partial b_g}{\partial T} \right)_{ij}^{n+1,k,(0)} \frac{\phi_j^{n+1,k+\frac{1}{2},(0)} - \phi_i^{n+1,k+\frac{1}{2},(0)}}{|\mathbf{x}_j - \mathbf{x}_i|} |S_{ij}| \right). \end{aligned} \quad (4.25)$$

Using the relations: $\beta = \frac{C_v}{4acT^3}$, $\phi = acT^4$, $\sum_{g=1}^G b_g = 1$, $\sum_{g=1}^G \frac{\partial B_g}{\partial T} = \frac{4acT^3}{4\pi}$, and $b_g + \frac{T}{4} \frac{\partial b_g}{\partial T} = \frac{4\pi}{4acT^3} \frac{\partial B_g}{\partial T}$, we have

$$\begin{aligned} & \left(\frac{C_v}{4 \left(T_i^{n+1,k,(0)} \right)^3} + a \right) \frac{\left(T_i^{n+1,k+\frac{1}{2},(0)} \right)^4 - \left(T_i^{n,(0)} \right)^4}{\Delta t} \\ & = \frac{1}{\Delta V_i} \sum_{j \in \mathcal{N}_i} \left(\frac{ac}{3\sigma_{R,ij}^{n+1,k,(0)}} \frac{\left(T_j^{n+1,k+\frac{1}{2},(0)} \right)^4 - \left(T_i^{n+1,k+\frac{1}{2},(0)} \right)^4}{|\mathbf{x}_j - \mathbf{x}_i|} |S_{ij}| \right), \end{aligned} \quad (4.26)$$

where the Rosseland mean opacity is defined as:

$$\frac{1}{\sigma_{R,ij}^{n+1,k,(0)}} = \left(\frac{\sum_{g=1}^G \frac{1}{\sigma_g} \frac{\partial B_g}{\partial T}}{\sum_{g=1}^G \frac{\partial B_g}{\partial T}} \right)_{ij}^{n+1,k,(0)}.$$

This provides a consistent approximation to the diffusion equation (4.22). Note that (4.26) remains valid only when the equilibrium condition: $\sum_{g=1}^G \rho_{g,i}^{n,(0)} = \sum_{g=1}^G b_{g,i}^{n,(0)} \phi_i^{n,(0)}$ is satisfied. As both quantities are computed via the Monte Carlo solver, the equilibrium property of the MC method is necessary, which will be demonstrated later.

In the correction step (3.21), with the scale (4.2), we have the scheme:

$$T_i^{n+1,k+1} + \frac{a}{C_v} \sum_{g=1}^G \chi_{g,i}^{n+1,k+\frac{1}{2}} b_{g,i}^{n+1,k+1} (T_i^{n+1,k+1})^4 - A_i = 0, \quad (4.27)$$

where

$$A_i = T_i^n + \frac{\Delta t}{C_v} \sum_{g=1}^G \chi_{g,i}^{n+1,k+\frac{1}{2}} \left(\frac{1}{c\Delta t} \rho_{g,i}^n - \frac{1}{\varepsilon \Delta V_i} \sum_{j \in \mathcal{N}_i} F_{g,ij}^{C,n+1,k+\frac{1}{2}} \right) \\ + \frac{\Delta t}{C_v} \sum_{g=1}^G \chi_{g,i}^{n+1,k+\frac{1}{2}} \left(\frac{1}{\varepsilon \Delta V_i} \sum_{j \in \mathcal{N}_i} D_{g,ij}^{n+1,k+\frac{1}{2}} \frac{\phi_j^{n+1,k+\frac{1}{2}} - \phi_i^{n+1,k+\frac{1}{2}}}{|\mathbf{x}_j - \mathbf{x}_i|} |S_{ij}| \right).$$

In the asymptotic limit $\varepsilon \rightarrow 0$, application of the Chapman-Enskog expansion yields, through analogous arguments to those previously established:

$$\frac{C_v}{\Delta t} (T_i^{n+1,k+1,(0)} - T_i^{n,(0)}) + a \frac{(T_i^{n+1,k+1,(0)})^4 - (T_i^{n,(0)})^4}{\Delta t} \\ = \frac{1}{\Delta V_i} \sum_{j \in \mathcal{N}_i} \left(\frac{ac}{3\sigma_{R,ij}^{n+1,k+\frac{1}{2},(0)}} \frac{(T_j^{n+1,k+\frac{1}{2},(0)})^4 - (T_i^{n+1,k+\frac{1}{2},(0)})^4}{|\mathbf{x}_j - \mathbf{x}_i|} |S_{ij}| \right), \quad (4.28)$$

where the Rosseland mean opacity is defined as:

$$\frac{1}{\sigma_{R,ij}^{n+1,k+\frac{1}{2},(0)}} = \left(\frac{\sum_{g=1}^G \frac{1}{\sigma_g} \frac{\partial B_g}{\partial T}}{\sum_{g=1}^G \frac{\partial B_g}{\partial T}} \right)_{ij}^{n+1,k+\frac{1}{2},(0)}.$$

This provides a consistent approximation to the diffusion equation (4.23). \square

For simplicity, we restrict our analysis to the one-dimensional case with a uniform cell V_i with length Δx in subsequent discussions.

Proposition 4.4. *When ε tends to 0, the solutions of the microscopic Monte Carlo solver can capture the equilibrium diffusion limit (4.4).*

Proof. Consider the systems

$$\frac{\varepsilon^2}{c} \frac{\partial I_g}{\partial t} + \varepsilon \mu \frac{\partial I_g}{\partial x} = \sigma_g B_g - \sigma_g I_g, \quad g = 1, \dots, G, \quad (4.29a)$$

$$\varepsilon^2 C_v \frac{\partial T}{\partial t} = \sum_{g=1}^G \sigma_g (\rho_g - 4\pi B_g). \quad (4.29b)$$

We now perform a Chapman-Enskog expansion and compare terms that are the same order in ε .

The $O(1)$ equation for (4.29a) is

$$I_g^{(0)} = B_g^{(0)}, \quad g = 1, \dots, G, \quad (4.30)$$

Integrating (4.34) over the angular variables yields

$$\rho_g^{(0)} = 4\pi B_g^{(0)}, \quad g = 1, \dots, G. \quad (4.31)$$

The $O(\varepsilon)$ equation for (4.29a) is

$$\mu \frac{\partial I_g^{(0)}}{\partial x} + \sigma_g I_g^{(1)} = \sigma_g B_g^{(1)}, \quad g = 1, \dots, G, \quad (4.32)$$

substituting (4.30) into (4.32), we can get

$$I_g^{(1)} = -\frac{1}{\sigma_g} \mu \frac{\partial B_g^{(0)}}{\partial x} + B_g^{(1)}, \quad g = 1, \dots, G. \quad (4.33)$$

The $O(\varepsilon^2)$ equation for (4.29a) is

$$\frac{1}{c} \frac{\partial I_g^{(0)}}{\partial t} + \mu \frac{\partial I_g^{(1)}}{\partial x} = \sigma_g B_g^{(2)} - \sigma_g I_g^{(2)}, \quad g = 1, \dots, G, \quad (4.34)$$

The $O(\varepsilon^2)$ equation for (4.29b) is

$$C_v \frac{\partial}{\partial t} T^{(0)} = \sum_{g=1}^G \sigma_g (\rho_g^{(2)} - 4\pi B_g^{(2)}), \quad (4.35)$$

Up to now, the asymptotic analysis was performed without considering the discretized formulation of the emission source $(B_{tilt})_{g,i}^{(0)}$. From the tilting source definition in (3.33), we obtain the second-order accurate approximation:

$$B_{g,i}^{(0)} = (B_{tilt})_{g,i}^{(0)} + O(\Delta x^2). \quad (4.36)$$

Consequently, the $O(\varepsilon)$ equation in (4.29a) takes the modified form:

$$\begin{aligned} I_{g,i}^{(1)} &= -\frac{1}{\sigma_g} \mu \frac{\partial (B_{tilt})_{g,i}^{(0)}}{\partial x} + B_{g,i}^{(1)} \\ &= B_{g,i}^{(1)} - \begin{cases} \frac{1}{\sigma_g} \mu \frac{B_{g,i}^{(0)} - B_{g,i-1}^{(0)}}{\Delta x} (x - x_i), & \text{if } \mu < 0, \\ \frac{1}{\sigma_g} \mu \frac{B_{g,i+1}^{(0)} - B_{g,i}^{(0)}}{\Delta x} (x - x_i), & \text{if } \mu > 0. \end{cases} \end{aligned} \quad (4.37)$$

By upwind principle, we have

$$I_{g,i+\frac{1}{2}}^{(1)} = \begin{cases} I_{g,i}, & \text{if } \mu > 0, \\ I_{g,i+1}, & \text{if } \mu < 0. \end{cases} \quad (4.38)$$

By integrating the the $O(\varepsilon^2)$ equation (4.34) over the cell V_i and angle, then summing over all groups while applying (4.31) and (4.35), we obtain

$$\frac{1}{c} \frac{\partial}{\partial t} \left(\sum_{g=1}^G 4\pi B_{g,i}^{(0)} \right) + C_v \frac{\partial}{\partial t} T^{(0)} = \frac{1}{\Delta x} \sum_{g=1}^G (F_{g,i+\frac{1}{2}}^{(1)} - F_{g,i-\frac{1}{2}}^{(1)}), \quad (4.39)$$

with the flux $F_{g,i+\frac{1}{2}}^{(1)}$ given by:

$$\begin{aligned}
F_{g,i+\frac{1}{2}}^{(1)} &= 2\pi \int_{-1}^1 \mu I_{g,i+\frac{1}{2}}^{(1)} d\mu \\
&= 2\pi \left(\int_{-1}^0 \mu I_{g,i+1}^{(1)} d\mu + \int_0^1 \mu I_{g,i}^{(1)} d\mu \right) \\
&= -2\pi \left(\int_{-1}^0 \frac{\mu^2}{\sigma_{g,i+1}} \frac{\partial (B_{tilt})_{g,i+1}^{(0)}}{\partial x} d\mu + \int_0^1 \frac{\mu^2}{\sigma_{g,i}} \frac{\partial (B_{tilt})_{g,i}^{(0)}}{\partial x} d\mu \right) \\
&= -\frac{1}{2} \left(\int_{-1}^0 \frac{4\pi\mu^2}{\sigma_{g,i+1}} \frac{B_{g,i+1}^{(0)} - B_{g,i}^{(0)}}{\Delta x} d\mu + \int_0^1 \frac{4\pi\mu^2}{\sigma_{g,i}} \frac{B_{g,i+1}^{(0)} - B_{g,i}^{(0)}}{\Delta x} d\mu \right) \\
&= -\frac{4\pi}{3\sigma_{g,i+\frac{1}{2}}} \frac{B_{g,i+1}^{(0)} - B_{g,i}^{(0)}}{\Delta x},
\end{aligned} \tag{4.40}$$

where $\sigma_{g,i+\frac{1}{2}}$ is the harmonic average of $\sigma_{g,i}$. Substituting the relation $\sum_{g=1}^G 4\pi B_{g,i}^{(0)} = ac(T_i^{(0)})^4$, we have

$$a \frac{\partial}{\partial t} (T_i^{(0)})^4 + C_v \frac{\partial}{\partial t} T_i^{(0)} = \frac{1}{\Delta x} \sum_{g=1}^G \left(\frac{4\pi}{3\sigma_{g,i+\frac{1}{2}}} \frac{B_{g,i+1}^{(0)} - B_{g,i}^{(0)}}{\Delta x} - \frac{4\pi}{3\sigma_{g,i-\frac{1}{2}}} \frac{B_{g,i}^{(0)} - B_{g,i-1}^{(0)}}{\Delta x} \right). \tag{4.41}$$

Therefore, a standard implicit diffusion scheme for (4.4) can be obtained. \square

5. Numerical Results

In this section, we present a series of numerical experiments to demonstrate the capability and effectiveness of the proposed method, termed Effective Monte Carlo (EMC). We compare EMC with the state-of-the-art Implicit Monte Carlo (IMC) method [11]. It is worth noting that while numerous acceleration techniques, variance reduction strategies, and code optimizations have been developed for IMC, our comparisons are limited to the version incorporating only *continuous energy deposition* as described in [11]. For each numerical test, the IMC method employs the same time step, mesh size, and number of particles as the EMC method.

In the following examples, the units are defined as follows: length in centimeters (cm), time in nanoseconds (ns), temperature in kilo electron-volts (keV), and energy in 10^9 Joules (GJ). Under these units, the speed of light c is 29.98 cm/ns and the radiation constant a is 0.01372 GJ/cm³/keV⁴. All numerical tests use 2,000,000 MC particles unless otherwise specified. The reference CFL number is determined by

$$\text{CFL} = \frac{c\Delta t}{\min(\Delta x, \Delta y)}.$$

5.1. Infinite medium problem (Test of variance)

In this example, we compare the Figure of Merit (FOM) between the EMC and IMC methods. The problem setup is similar to that described in [49]. The FOM for Monte Carlo simulations is defined as

$$\text{FOM} = \frac{1}{\text{Var} \cdot t},$$

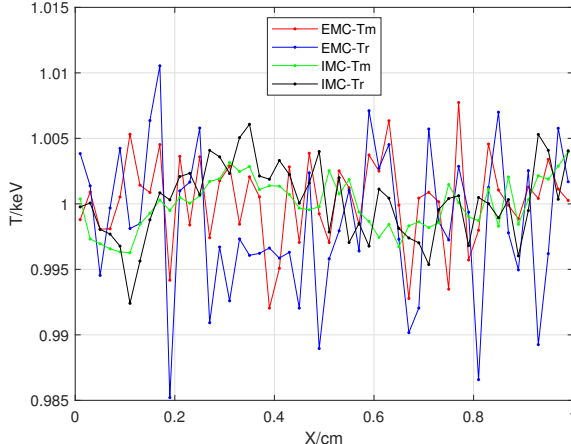


Figure 5.1: Comparison of the material and radiation temperatures using the EMC and IMC methods at $t = 1.0$ ns, with $\Delta t = 0.0025$ ns (CFL ≈ 15) for the infinite medium problem.

where Var represents the variance of the estimate and t denotes the CPU time. A higher FOM indicates better computational efficiency, corresponding to lower variance and reduced computation time.

We consider a steady-state, infinite medium problem with an initial equilibrium temperature of $T_{m,0} = T_{r,0} = 1.0$ keV. The system is modeled as a one-dimensional slab of thickness 1.0 cm with reflecting boundary conditions. The opacity is defined by

$$\sigma = \frac{300}{T^3} \text{ cm}^{-1},$$

and the heat capacity is given by

$$C_v = 0.3 \text{ GJ/keV/cm}^3.$$

The exact solution predicts that the medium remains at its initial temperature throughout the simulation. The computational domain is discretized into 50 uniform spatial cells, using a fixed time step of $\Delta t = 0.0025$ ns (CFL ≈ 15). The simulation is run until a final time of $t = 1.0$ ns.

The spatial variations of material and radiation temperatures at $t = 1.0$ ns are shown in Figure 5.1 for both the EMC and IMC methods. It can be seen that the variations in the EMC method are more pronounced than those in the IMC method. This is attributed to the absence of effective scattering in EMC. Nevertheless, the EMC method is significantly faster due to shorter particle lifetimes. To reach the simulation time of $t = 1.0$ ns, the IMC method requires 669 s, whereas the EMC method only takes 53 s as shown in Table 5.1. The FOMs for both methods are presented in Figure 5.2, showing that EMC achieves substantially higher FOMs for both material and radiation temperatures.

Example 5.1	EMC (s)	IMC (s)
FOM	54	606

Table 5.1: Comparison of CPU time using the EMC and IMC methods for Example 5.1 (in seconds).

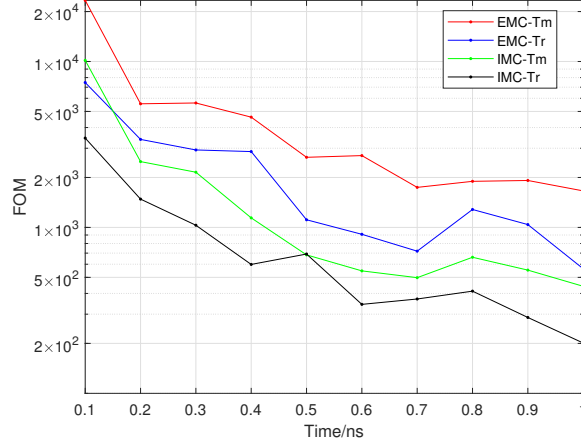


Figure 5.2: Figure of Merit for the material and radiation temperatures using the EMC and IMC methods.

5.2. Marshark wave problems

For this example, we consider the frequency-dependent Marshak wave problems [47, 50, 8, 51]. These consist of several one-dimensional cases with varying optical depths: optically thin, optically thick, and a combination of both.

In all test problems, the initial temperature is in equilibrium, given by $T_{r,0} = T_{m,0} = 10^{-3}$ keV. The frequency-dependent opacity in each region is given by

$$\sigma(x, \nu, T) = \frac{\sigma_0(x)}{(h\nu)^3 \sqrt{kT}} \text{ cm}^{-1},$$

and the heat capacity is set to

$$C_v = 0.1 \text{ GJ/keV/cm}^3.$$

To represent the frequency-dependent opacity, we employ 25 frequency groups spaced logarithmically between 10^{-3} keV and 100 keV.

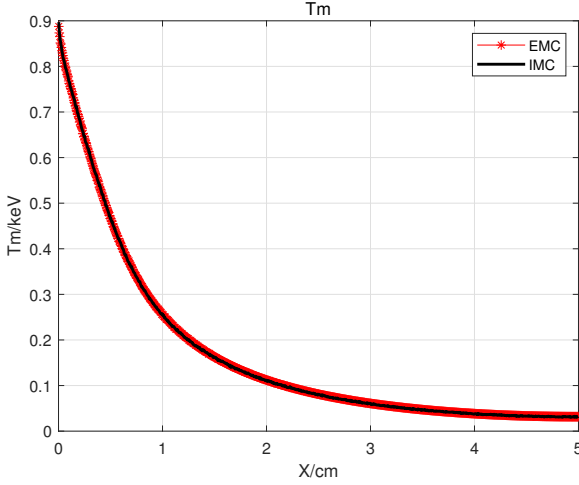
At the left boundary, the incident intensity follows a Planckian distribution with a temperature of 1.0 keV, while a reflective boundary condition is applied at the right boundary. The simulation is run until a final time of $t = 1.0$ ns.

5.2.1. Homogeneous problems

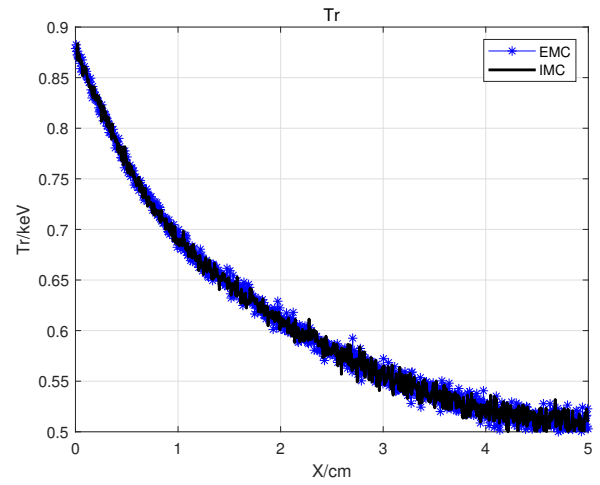
Two homogeneous test cases are considered in a computational domain of thickness 5.0 cm, with opacity values given by

$$\sigma_0 = 10 \text{ keV}^{7/2}/\text{cm}, \quad \sigma_0 = 1000 \text{ keV}^{7/2}/\text{cm}.$$

The spatial domain is discretized using a uniform mesh with a cell size of $\Delta x = 0.005$ cm. The time step is set to $\Delta t = 0.0025$ ns (CFL ≈ 15). Figure 5.3 and Figure 5.4 present the material and radiation temperatures computed using both the EMC and IMC methods. The results show good agreement between the two approaches. As shown in Figure 5.4, which corresponds to the optically thick case, the temperature profiles are noisier. However, EMC demonstrates significantly better computational efficiency compared to IMC in the optically thick regime, as indicated in Table 5.2.

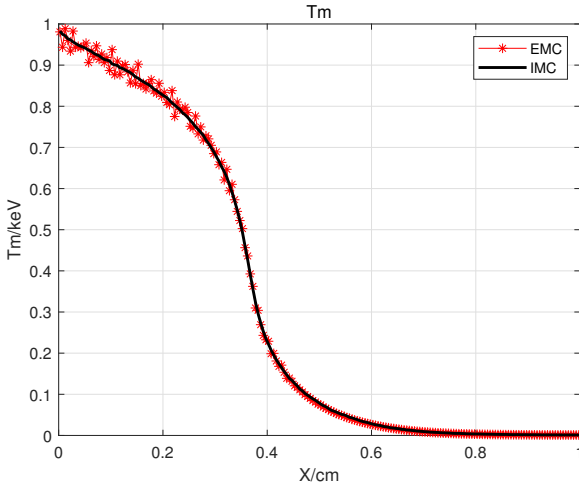


(a) Material temperature.

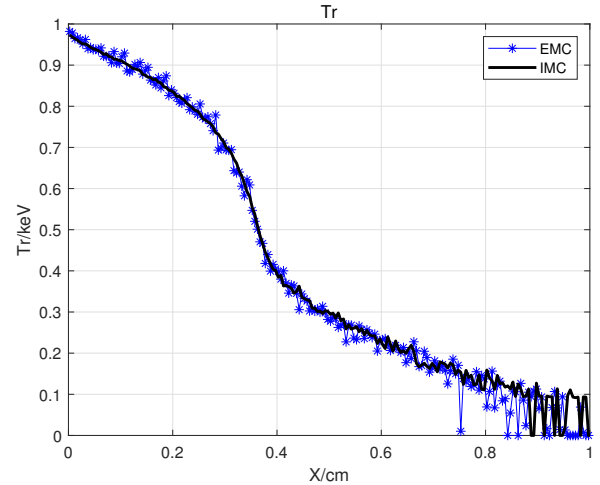


(b) Radiation temperature.

Figure 5.3: Comparisons of the material and radiation temperatures using the EMC and IMC methods at $t = 1.0$ ns, with $\Delta t = 0.0025$ ns (CFL ≈ 15) for homogeneous Marshak wave problem when $\sigma_0 = 10 \text{ keV}^{7/2}/\text{cm}$.



(a) Material temperature.



(b) Radiation temperature.

Figure 5.4: Comparisons of the material and radiation temperatures using the EMC and IMC methods at $t = 1.0$ ns, with $\Delta t = 0.0025$ ns (CFL ≈ 15) for homogeneous Marshak wave problem when $\sigma_0 = 1000 \text{ keV}^{7/2}/\text{cm}$.

5.2.2. Heterogeneous problem A

The opacity profile in the computational domain is given by

$$\sigma_0(x) = \begin{cases} 10 \text{ keV}^{7/2}/\text{cm}, & 0 \text{ cm} < x < 2 \text{ cm}, \\ 1000 \text{ keV}^{7/2}/\text{cm}, & 2 \text{ cm} < x < 3 \text{ cm}. \end{cases}$$

The thickness of the computational domain is 3.0 cm, and the spatial mesh size is

$$\Delta x = \begin{cases} 0.02 \text{ cm}, & 0 \text{ cm} < x < 2 \text{ cm}, \\ 0.005 \text{ cm}, & 2 \text{ cm} < x < 3 \text{ cm}. \end{cases}$$

The time step is set to $\Delta t = 0.00125$ ns (CFL ≈ 8). This test problem evaluates the ability of our methods to handle a sharp transition from an optically thin to an optically thick regime. The simulation runs up to a final time of 1.0 ns. Figure 5.5 presents the EMC and IMC results, which show good agreement.

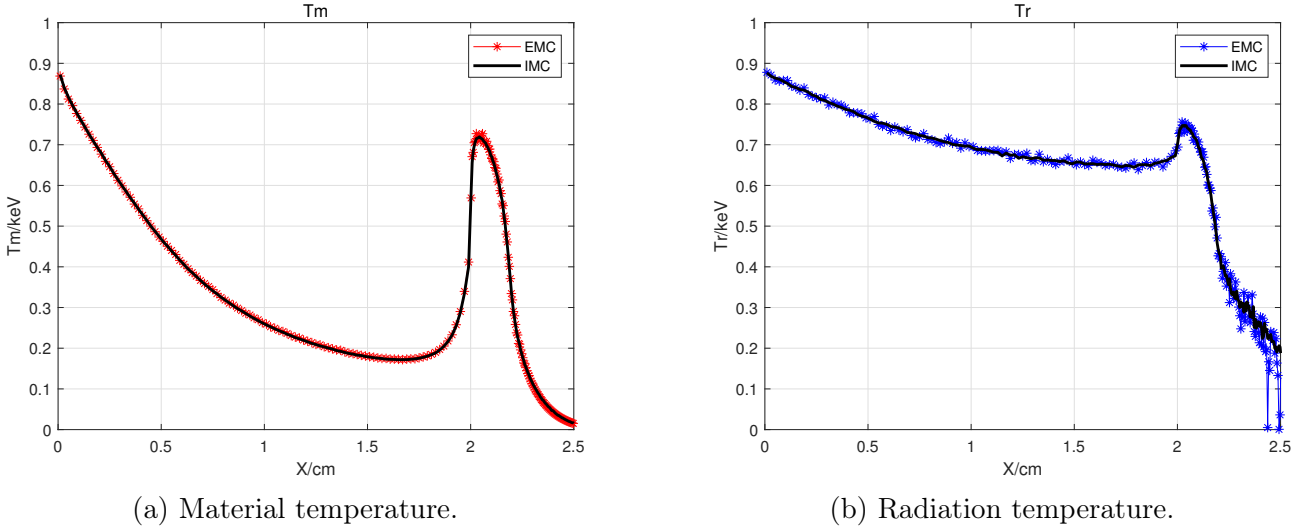


Figure 5.5: Comparisons of the material and radiation temperatures using the EMC and IMC methods at $t = 1.0$ ns, with $\Delta t = 0.00125$ ns (CFL ≈ 8) for heterogeneous Marshak wave problem A.

5.2.3. Heterogeneous problem B

The opacity profile in the computational domain is given by

$$\sigma_0(x) = \begin{cases} 1000 \text{ keV}^{7/2}/\text{cm}, & 0 \text{ cm} < x < 0.5 \text{ cm}, \\ 10 \text{ keV}^{7/2}/\text{cm}, & 0.5 \text{ cm} < x < 1.5 \text{ cm}. \end{cases}$$

The thickness of the computational domain is 1.5 cm, and the spatial mesh size is

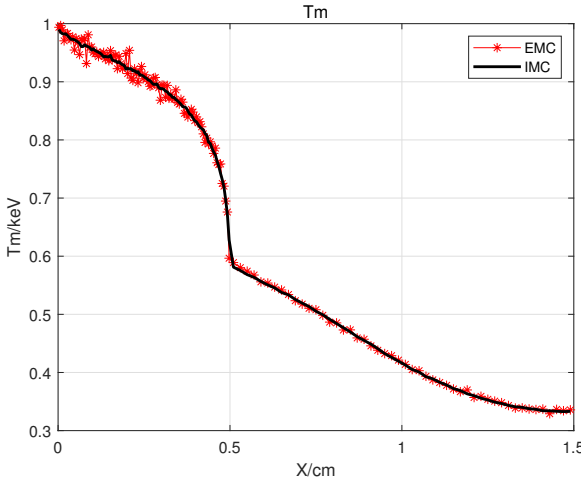
$$\Delta x = \begin{cases} 0.005 \text{ cm}, & 0 \text{ cm} < x < 0.5 \text{ cm}, \\ 0.02 \text{ cm}, & 0.5 \text{ cm} < x < 1.5 \text{ cm}. \end{cases}$$

The time step is set to $\Delta t = 0.00125$ ns (with CFL ≈ 8). This problem assesses the capability of our methods to handle a sharp transition from an optically thick to an optically thin regime over a long simulation time. The simulation runs up to a final time of 5.0 ns, making it particularly challenging due to the extended duration. Nevertheless, Figure 5.6 demonstrates strong agreement between the two approaches, especially near the thick-to-thin interface. Although the temperature exhibits more noise in the optically thick regime, Table 5.2 demonstrates that EMC achieves excellent computational efficiency.

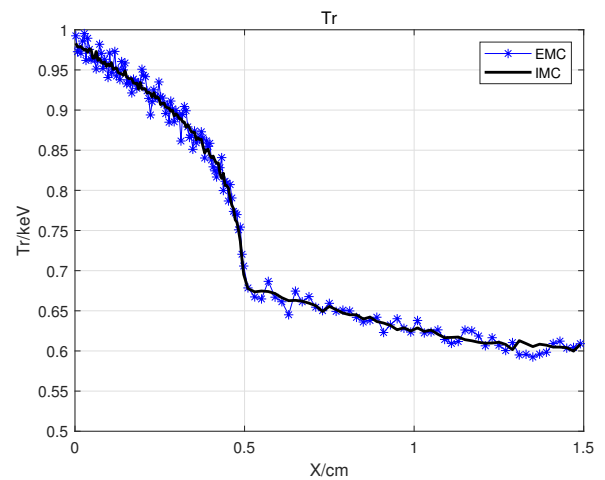
5.3. Larsen's problem

Next, we consider the frequency-dependent, multi-material Larsen's problem [52, 30, 51]. To model the frequency-dependent opacity, we employ 50 frequency groups spaced logarithmically between 10^{-5} keV and 10 keV. The frequency-dependent opacity in each region is given by

$$\sigma(x, \nu, T) = \sigma_0(x) \frac{1 - e^{-h\nu/kT}}{(h\nu)^3} \text{ cm}^{-1},$$



(a) Material temperature.



(b) Radiation temperature.

Figure 5.6: Comparisons of the material and radiation temperatures using the EMC and IMC methods at $t = 1.0$ ns, with $\Delta t = 0.00125$ ns (CFL ≈ 8) for heterogeneous Marshak wave problem B.

Example 5.2	EMC (s)	IMC (s)
$\sigma_0 = 10$	146	293
$\sigma_0 = 1000$	152	9125
Heterogeneous A	160	3008
Heterogeneous B	930	32762

Table 5.2: Comparison of CPU time using the EMC and IMC methods for Example 5.2 (in seconds).

where the spatially varying coefficient $\sigma_0(x)$ is given by

$$\sigma_0(x) = \begin{cases} 1 \text{ keV}^{2/7}/\text{cm}, & 0 < x < 2 \text{ cm}, \\ 1000 \text{ keV}^{2/7}/\text{cm}, & 2 < x < 3 \text{ cm}, \\ 1 \text{ keV}^{2/7}/\text{cm}, & 3 < x < 4 \text{ cm}. \end{cases}$$

The heat capacity is specified as

$$C_v = 0.05109 \text{ GJ/keV/cm}^3.$$

The system is initialized in thermal equilibrium, with both radiation and material temperatures set to $T_{r,0} = T_{m,0} = 10^{-3}$ keV. A Planckian surface source at 1.0 keV is applied at the left boundary to initiate the transient. The simulation runs until a final time of 0.9 ns. The spatial domain is divided into three regions with non-uniform mesh sizes:

$$\Delta x = \begin{cases} 0.2 \text{ cm}, & 0 < x < 2 \text{ cm}, \\ 0.02 \text{ cm}, & 2 < x < 3 \text{ cm}, \\ 0.1 \text{ cm}, & 3 < x < 4 \text{ cm}. \end{cases}$$

The fixed time step $\Delta t = 0.005$ ns (CFL ≈ 8) is used throughout the simulation.

This problem evaluates the ability of our methods to accurately capture the sharp transition from an optically thick to an optically thin regime. The simulation runs up to a final time of 0.9 ns. Nevertheless, Figure 5.7 demonstrates strong agreement between the two approaches, especially near the thick-to-thin interface. Table 5.3 demonstrates that EMC achieves excellent computational efficiency.

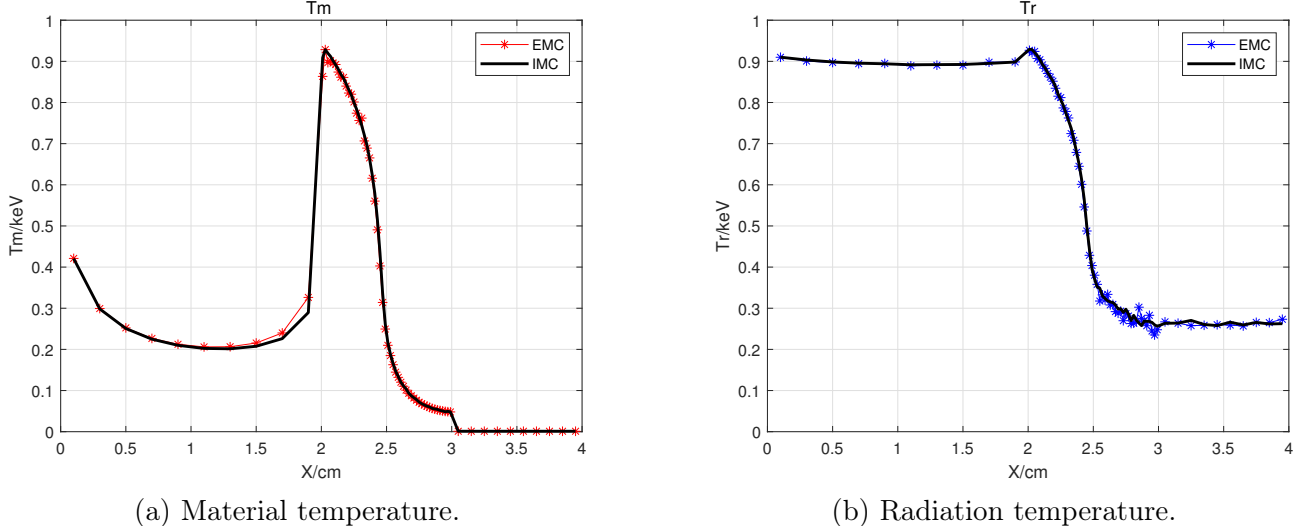


Figure 5.7: Comparisons of the material and radiation temperatures using the EMC and IMC methods at $t = 0.9$ ns, with $\Delta t = 0.005$ ns (CFL ≈ 8) for Larsen's problem.

Example 5.3	EMC (s)	IMC (s)
Larsen's Pb.	24	404

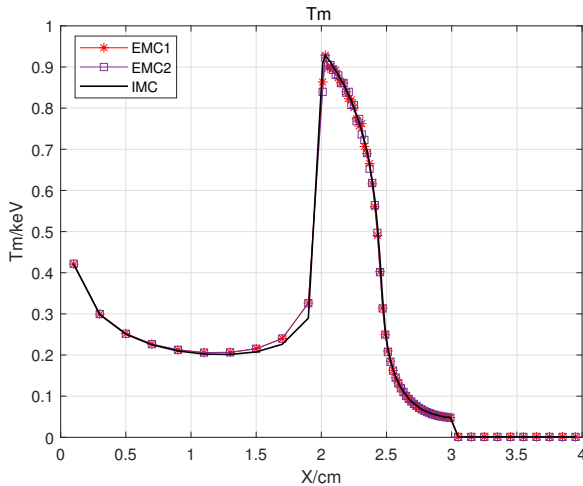
Table 5.3: Comparison of CPU time using the EMC and IMC methods for Example 5.3 (in seconds).

5.3.1. Test of different weight functions

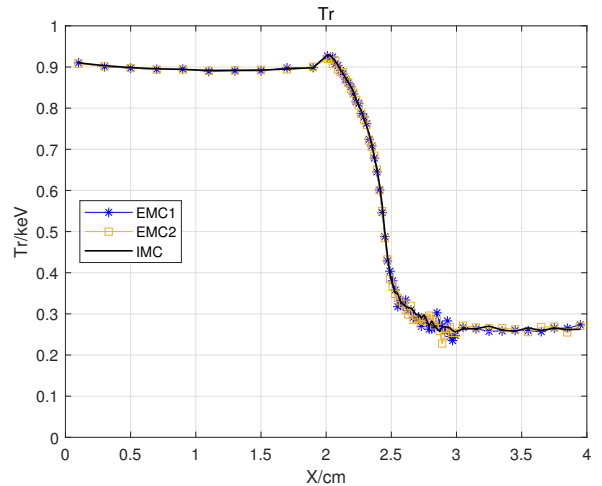
We use Larsen's problem to demonstrate the necessity of modifying the original model using (2.23) and the fact that the proposed scheme is generally insensitive to the specific choice of the weight function θ_g . The candidate weight functions considered are $\theta_g = e^{-c\sigma_g(t-t^n)}$ and $\theta_g = 1 - e^{-1/(c\sigma_g(t-t^n))}$, referred to as EMC1 and EMC2, respectively. When the time step is $\Delta t = 0.005$ ns (CFL ≈ 8), the results shown in Figure 5.8 indicate that the solutions obtained with EMC1 and EMC2 are in close agreement. In contrast, using $\theta_g = 0$, which corresponds to the unmodified model given in (2.22), leads to failure in the convergence of the nonlinear iteration for the macroscopic system.

5.4. Frequency-dependent hohlraum problem

For the final example, we study the hohlraum problem for the multi-frequency radiative transfer equation. The setup of this problem is similar as that studied in [45, 53]. To represent the frequency-dependent opacity, our method employs 50 frequency groups spaced logarithmically between 10^{-5} keV and 10 keV.



(a) Material temperature.



(b) Radiation temperature.

Figure 5.8: Comparisons of the material and radiation temperatures using the EMC method with different weight functions and the IMC method at $t = 0.9$ ns, with $\Delta t = 0.005$ ns ($\text{CFL} \approx 8$) for Larsen's problem.

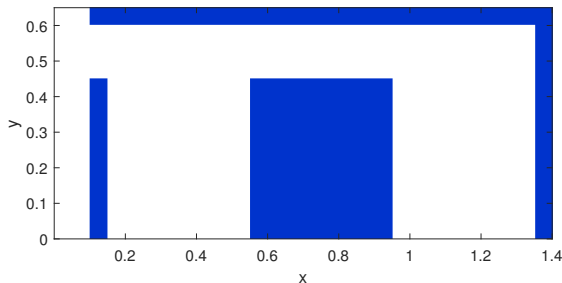


Figure 5.9: The hohlraum problem. The blue regions are where $(x, y) \in [0.1, 0.15] \times [0, 0.45]$, and $(x, y) \in [0.55, 0.95] \times [0, 0.45]$, $(x, y) \in [0.1, 1.4] \times [0.6, 0.65]$, and $(x, y) \in [1.35, 1.4] \times [0, 0.65]$.

The layout of the problem is illustrated in Figure 5.9. The computational domain spans $[0 \text{ cm}, 1.4 \text{ cm}] \times [0 \text{ cm}, 0.65 \text{ cm}]$, where the white regions represent near-vacuum. We assume an absorption coefficient of

$$\sigma = 10^{-8} \text{ cm}^{-1},$$

and a specific heat capacity of

$$C_v = 10^{-4} \text{ GJ/keV/cm}^3,$$

for the white regions. The blue regions are filled with material that follows the frequency-dependent opacity relation

$$\sigma(x, \nu, T) = 1000 \frac{1 - e^{-h\nu/kT}}{(h\nu)^3} \text{ cm}^{-1},$$

with a specific heat capacity of

$$C_v = 0.3 \text{ GJ/keV/cm}^3.$$

The initial temperature is in equilibrium, given by $T_{r,0} = T_{m,0} = 10^{-3} \text{ keV}$. A reflective boundary condition is imposed on the lower boundary. The left boundary is maintained with an angularly isotropic specific intensity corresponding to a 0.3 keV black body source. The upper and right boundaries are fixed at a specific intensity described by a Planckian distribution with temperature 10^{-3} keV .

The time step is set to $\Delta t = 0.0025 \text{ ns}$ ($\text{CFL} \approx 12$). A total of 6, 000, 000 particles is employed per time step. In [Figure 5.10](#), we present the radiation and material temperatures at time $t = 10.0 \text{ ns}$ obtained from the IMC and EMC solutions. We can see that the central block is heated non-uniformly and there is less radiation behind the block with respect to the source. The comparisons of material temperature along the diagnostic lines $y = 0.45 \text{ cm}$ and $y = 0.65 \text{ cm}$ are shown in [Figure 5.11](#), where the IMC and EMC results are generally consistent with each other. As shown in [Table 5.4](#), it takes the IMC method 96332 seconds to reach $t = 10.0 \text{ ns}$, whereas the EMC method takes only 17687 seconds, making it about five times faster for this example.

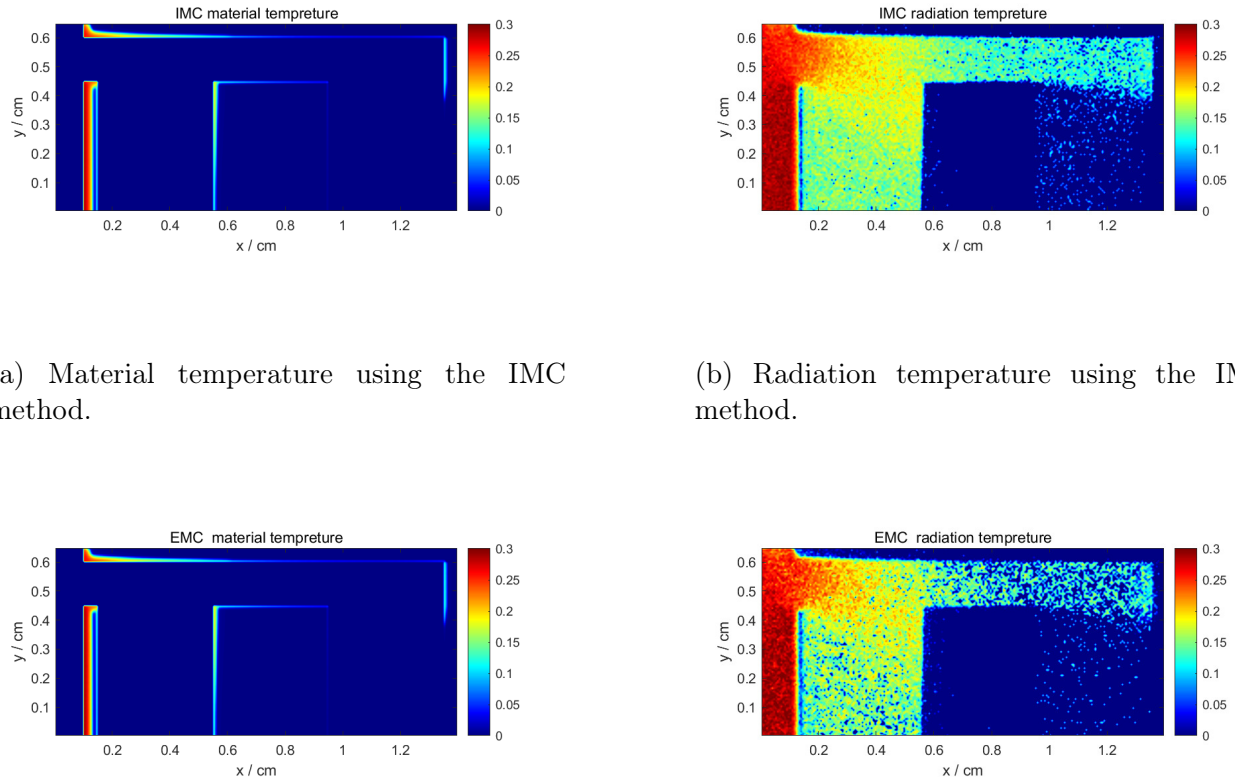
Example 5.4	EMC (s)	IMC (s)
Hohlraum Pb.	17687	96332

Table 5.4: Comparison of CPU time using the EMC and IMC methods for Example 5.4 (in seconds).

6. Conclusions and outlook

In this work, we develop an efficient AP MC method for frequency-dependent radiative transfer equations. By combining a multi-group frequency discretization with characteristic-based flux construction, we derive a micro-macro system which couples a low dimension convection-diffusion-type equation for macroscopic quantities with a high dimension transport equation for radiative intensity. This formulation enables the use of large time steps independent of the speed of light. A hybrid finite volume scheme is employed to efficiently solve the macroscopic equations, while a Picard iteration with a predictor-corrector strategy effectively manages the high-dimensional nonlinear coupling across both spatial and frequency dimensions. The resulting transport problem reduces to a tractable absorption-only system, which is solved using a particle-based MC method. The scheme has been formally proved to be AP. Numerical results confirm substantial efficiency gains over the IMC method, especially in optically thick regimes.

While our new approach requires much less CPU time, the absence of effective scattering leads to considerably higher noise compared to IMC under the same settings. Variance reduction techniques for the proposed method will be explored in future work.



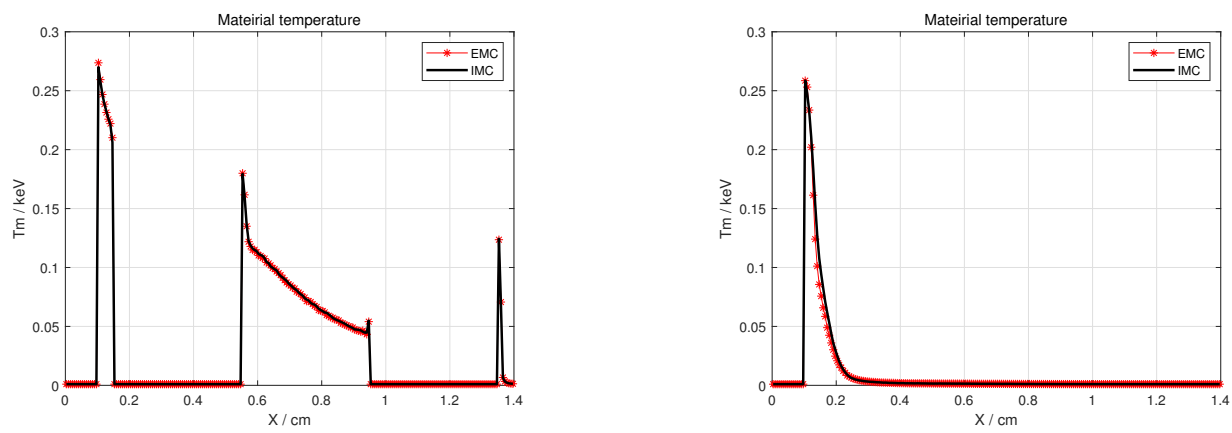
(a) Material temperature using the IMC method.

(b) Radiation temperature using the IMC method.

(c) Material temperature using the EMC method.

(d) Radiation temperature using the EMC method.

Figure 5.10: Comparisons of the material and radiation temperatures using the EMC and IMC methods at $t = 10.0$ ns, with $\Delta t = 0.0025$ ns ($\text{CFL} \approx 12$) for the frequency-dependent hohlraum problem.



(a) Material temperature along the line $y = 0.45$ cm.

(b) Material temperature along the line $y = 0.65$ cm.

Figure 5.11: Comparisons of the material temperature using the EMC and IMC methods at $t = 10.0$ ns for the frequency-dependent hohlraum problem.

Acknowledgements

References

- [1] Y. Shi, P. Song, T. Xiong, An efficient asymptotic preserving Monte Carlo method for radiative transfer equations, *Journal of Computational Physics* 493 (2023) 112483.
- [2] G. Zhang, H. Zhu, T. Xiong, Asymptotic preserving and uniformly unconditionally stable finite difference schemes for kinetic transport equations, *SIAM Journal on Scientific Computing* 45 (5) (2023) B697–B730.
- [3] G. C. Pomraning, *The equations of radiation hydrodynamics*, Courier Corporation, 2005.
- [4] W. H. Reed, Spherical harmonic solutions of the neutron transport equation from discrete ordinate codes, *Nuclear Science and Engineering* 49 (1) (1972) 10–19.
- [5] R. G. McClarren, J. P. Holloway, T. A. Brunner, On solutions to the P_n equations for thermal radiative transfer, *Journal of Computational Physics* 227 (5) (2008) 2864–2885.
- [6] R. G. McClarren, C. D. Hauck, Robust and accurate filtered spherical harmonics expansions for radiative transfer, *Journal of Computational Physics* 229 (16) (2010) 5597–5614.
- [7] M. L. Adams, Subcell balance methods for radiative transfer on arbitrary grids, *Transport Theory and Statistical Physics* 26 (4-5) (1997) 385–431.
- [8] W. Sun, S. Jiang, K. Xu, S. Li, An asymptotic preserving unified gas kinetic scheme for frequency-dependent radiative transfer equations, *Journal of Computational Physics* 302 (2015) 222–238.
- [9] T. Xiong, W. Sun, Y. Shi, P. Song, High order asymptotic preserving discontinuous Galerkin methods for gray radiative transfer equations, *Journal of Computational Physics* 463 (2022) 111308.
- [10] T. A. Brunner, Forms of Approximate Radiation Transport, Tech. rep., Sandia National Lab. (SNL-NM), Albuquerque, NM (United States); Sandia National Lab. (SNL-CA), Livermore, CA (United States) (2002).
- [11] J. A. Fleck Jr, J. Cummings Jr, An implicit Monte Carlo scheme for calculating time and frequency dependent nonlinear radiation transport, *Journal of Computational Physics* 8 (3) (1971) 313–342.
- [12] J. A. Fleck, E. H. Canfield, A random walk procedure for improving the computational efficiency of the implicit Monte Carlo method for nonlinear radiation transport, *Journal of Computational Physics* 54 (3) (1984) 508–523.
- [13] J. Giorla, R. Sentis, A random walk method for solving radiative transfer equations, *Journal of Computational Physics* 70 (1) (1987) 145–165.
- [14] K. P. Keady, An improved random walk algorithm for the implicit Monte Carlo method, *Journal of Computational Physics* (2017).

- [15] J. D. Densmore, T. J. Urbatsch, T. M. Evans, M. W. Buksas, A hybrid transport-diffusion method for Monte Carlo radiative-transfer simulations, *Journal of Computational Physics* 222 (2) (2007) 485–503.
- [16] J. D. Densmore, K. G. Thompson, T. J. Urbatsch, A hybrid transport-diffusion Monte Carlo method for frequency-dependent radiative-transfer simulations, *Journal of Computational Physics* 231 (20) (2012) 6924–6934.
- [17] M. A. Cleveland, N. A. Gentile, T. S. Palmer, An extension of implicit Monte Carlo diffusion: Multigroup and the difference formulation, *Journal of Computational Physics* 229 (16) (2010) 5707–5723.
- [18] N. A. Gentile, Implicit Monte Carlo diffusion—an acceleration method for Monte Carlo time-dependent radiative transfer simulations, *Journal of Computational Physics* 172 (2) (2001) 543–571.
- [19] M. A. Cleveland, N. Gentile, Mitigating teleportation error in frequency-dependent hybrid implicit Monte Carlo diffusion methods, *Journal of Computational and Theoretical Transport* 43 (1-7) (2014) 6–37.
- [20] J. D. Densmore, Interface methods for hybrid Monte Carlo-diffusion radiation-transport simulations, *Annals of Nuclear Energy* 33 (4) (2006) 343–353.
- [21] L. Chacon, G. Chen, D. A. Knoll, C. Newman, H. Park, W. Taitano, J. A. Willert, G. Womeldorff, Multiscale high-order/low-order (HOLO) algorithms and applications, *Journal of Computational Physics* 330 (2017) 21–45.
- [22] B. C. Yee, A. B. Wollaber, T. S. Haut, H. Park, A stable 1D multigroup high-order low-order method, *Journal of Computational and Theoretical Transport* 46 (1) (2017) 46–76.
- [23] H. Park, L. Chacón, A. Matsekh, G. Chen, A multigroup moment-accelerated deterministic particle solver for 1-D time-dependent thermal radiative transfer problems, *Journal of Computational Physics* 388 (2019) 416–438.
- [24] S. R. Bolding, M. A. Cleveland, J. E. Morel, A high-order low-order algorithm with exponentially convergent Monte Carlo for thermal radiative transfer, *Nuclear Science and Engineering* 185 (1) (2017) 159–173.
- [25] E. W. Larsen, J. E. Morel, W. F. Miller Jr, Asymptotic solutions of numerical transport problems in optically thick, diffusive regimes, *Journal of Computational Physics* 69 (2) (1987) 283–324.
- [26] E. W. Larsen, J. E. Morel, Asymptotic solutions of numerical transport problems in optically thick, diffusive regimes II, *Journal of Computational Physics* 83 (1) (1989) 212–236.
- [27] A. Klar, An asymptotic-induced scheme for nonstationary transport equations in the diffusive limit, *SIAM journal on Numerical Analysis* 35 (3) (1998) 1073–1094.
- [28] S. Jin, Asymptotic-preserving schemes for multiscale physical problems, *Acta Numerica* 31 (2022) 415–489.

- [29] Y. Shi, P. Song, W. Sun, An asymptotic preserving unified gas kinetic particle method for radiative transfer equations, *Journal of Computational Physics* 420 (2020) 109687.
- [30] W. Sun, S. Jiang, K. Xu, An asymptotic preserving unified gas kinetic scheme for gray radiative transfer equations, *Journal of Computational Physics* 285 (2015) 265–279.
- [31] W. Li, C. Liu, Y. Zhu, J. Zhang, K. Xu, Unified gas-kinetic wave-particle methods III: Multiscale photon transport, *Journal of Computational Physics* 408 (2020) 109280.
- [32] C. Liu, W. Li, Y. Wang, P. Song, K. Xu, An implicit unified gas-kinetic wave-particle method for radiative transport process, *Physics of Fluids* 35 (11) (2023).
- [33] X. Yang, Y. Zhu, C. Liu, K. Xu, Unified gas-kinetic wave-particle method for frequency-dependent radiation transport equation, *Journal of Computational Physics* 522 (2025) 113587.
- [34] X. Xu, S. Jiang, W. Sun, A positive and asymptotic preserving filtered P_N method for the gray radiative transfer equations, *Journal of Computational Physics* 444 (2021) 110546.
- [35] X. Xu, S. Jiang, W. Sun, Spatial second-order positive and asymptotic preserving filtered P_N schemes for nonlinear radiative transfer equations, *Journal of Computational Physics* 508 (2024) 112985.
- [36] M. Tang, L. Wang, X. Zhang, Accurate front capturing asymptotic preserving scheme for nonlinear gray radiative transfer equation, *SIAM Journal on Scientific Computing* 43 (3) (2021) B759–B783.
- [37] H. Park, Toward asymptotic diffusion limit preserving high-order, low-order method, *Nuclear Science and Engineering* 194 (11) (2020) 952–970.
- [38] J. E. Morel, T. A. Wareing, K. Smith, A linear-discontinuous spatial differencing scheme for S_n radiative transfer calculations, *Journal of Computational Physics* 128 (2) (1996) 445–462.
- [39] K. Xu, J. C. Huang, A unified gas-kinetic scheme for continuum and rarefied flows, *Journal of Computational Physics* 229 (20) (2010) 7747–7764.
- [40] L. Mieussens, On the asymptotic preserving property of the unified gas kinetic scheme for the diffusion limit of linear kinetic models, *Journal of Computational Physics* 253 (2013) 138–156.
- [41] Y. Cai, G. Zhang, H. Zhu, T. Xiong, Asymptotic preserving semi-Lagrangian discontinuous Galerkin methods for multiscale kinetic transport equations, *Journal of Computational Physics* (2024) 113190.
- [42] Y. Shi, X. Han, W. Sun, P. Song, A continuous source tilting scheme for radiative transfer equations in implicit Monte Carlo, *Journal of Computational and Theoretical Transport* 50 (1) (2020) 1–26.
- [43] E. W. Larsen, A. Kumar, J. E. Morel, Properties of the implicitly time-differenced equations of thermal radiation transport, *Journal of Computational Physics* 238 (2013) 82–96.

- [44] X. Zhang, P. Song, Y. Shi, M. Tang, A fully asymptotic preserving decomposed multi-group method for the frequency-dependent radiative transfer equations, *Journal of Computational Physics* 491 (2023) 112368.
- [45] W. Li, C. Liu, P. Song, Unified gas-kinetic particle method for frequency-dependent radiation transport, *Journal of Computational Physics* 498 (2024) 112663.
- [46] A. B. Wollaber, Four decades of implicit Monte Carlo, *Journal of Computational and Theoretical Transport* 45 (1-2) (2016) 1–70.
- [47] J. D. Densmore, Asymptotic analysis of the spatial discretization of radiation absorption and re-emission in implicit Monte Carlo, *Journal of Computational Physics* 230 (4) (2011) 1116–1133.
- [48] E. Larsen, G. Pomraning, V. Badham, Asymptotic analysis of radiative transfer problems, *Journal of Quantitative Spectroscopy and Radiative Transfer* 29 (4) (1983) 285–310.
- [49] R. G. McClarren, T. J. Urbatsch, A modified implicit Monte Carlo method for time-dependent radiative transfer with adaptive material coupling, *Journal of Computational Physics* 228 (16) (2009) 5669–5686.
- [50] E. Steinberg, S. I. Heizler, Frequency-dependent discrete implicit Monte Carlo scheme for the radiative transfer equation, *Nuclear Science and Engineering* 197 (9) (2023) 2343–2355.
- [51] Y. Shi, A maximum principle preserving implicit Monte Carlo method for frequency-dependent radiative transfer equations, *Journal of Computational Physics* 495 (2023) 112552.
- [52] E. W. Larsen, A grey transport acceleration method for time-dependent radiative transfer problems, *Journal of Computational Physics* 78 (2) (1988) 459–480.
- [53] H. Hammer, H. Park, L. Chacon, A multi-dimensional, moment-accelerated deterministic particle method for time-dependent, multi-frequency thermal radiative transfer problems, *Journal of Computational Physics* 386 (2019) 653–674.

Appendix A. Newton iteration for the correction step

In the correction step (3.21), we are required to solve the nonlinear equation $\mathcal{F}(T_i^{n+1,k+1}) = 0$ for each cell, where the function $\mathcal{F}(T_i^{n+1,k+1})$ is defined as

$$\mathcal{F}(T_i^{n+1,k+1}) := T_i^{n+1,k+1} + \frac{a}{C_v} \sum_{g=1}^G \chi_{g,i}^{n+1,k+\frac{1}{2}} b_{g,i}^{n+1,k+1} (T_i^{n+1,k+1})^4 - A_i, \quad (\text{A.1})$$

with

$$A_i = T_i^n + \frac{\Delta t}{C_v} \sum_{g=1}^G \chi_{g,i}^{n+1,k+\frac{1}{2}} \left(\frac{1}{c\Delta t} \rho_{g,i}^n - \frac{1}{\Delta V_i} \sum_{j \in \mathcal{N}_i} \left(F_{g,ij}^{C,n+1,k+\frac{1}{2}} - F_{g,ij}^{D,n+1,k+\frac{1}{2}*} \right) \right). \quad (\text{A.2})$$

The derivative of $\mathcal{F}(T_i^{n+1,k+1})$ is given by

$$\mathcal{F}'(T_i^{n+1,k+1}) = 1 + \frac{4a}{C_v} \sum_{g=1}^G \chi_{g,i}^{n+1,k+\frac{1}{2}} \left(b_g + \frac{T}{4} \frac{\partial b_g}{\partial T} \right)_i^{n+1,k+1} (T_i^{n+1,k+1})^3. \quad (\text{A.3})$$

To solve for $T_i^{n+1,k+1}$, we employ the Newton iteration method:

$$T_i^{n+1,k+1,s+1} = T_i^{n+1,k+1,s} - \frac{\mathcal{F}(T_i^{n+1,k+1,s})}{\mathcal{F}'(T_i^{n+1,k+1,s})}, \quad (\text{A.4})$$

where the initial guess $T_i^{n+1,k+1,0}$ is taken from $T_i^{n+1,k+\frac{1}{2}}$ obtained in the prediction step.